Trigonal vs Nontrigonal Deformation from Octahedral Geometry in d^0 Metal Six-Coordination: Two Geometrical Isomers of [Metal tris(norbornane-*exo*-2,3-dithiolate)]$^-$ (Metal = Nb, Ta) and Their Interconversion

Kazuyuki Tatsumi,*,† Ichiro Matsubara,† Yoshihisa Inoue,† Akira Nakamura,*,† Kunio Miki,*,‡ and Nobutami Kasai*,‡

Contribution from the Department of Macromolecular Science, Faculty of Science, Osaka University, Toyonaka, Osaka 560, Japan, and Department of Applied Chemistry, Faculty of Engineering, Osaka University, Suita, Osaka 565, Japan. *Received March 30, 1989*

Abstract: The tris(norbornane-*exo*-2,3-dithiolate) complexes of Nb^V and Ta^V, [A][M(ndt)$_3$] (A = Ph_4P^+, Et_4N^+, *n*-Bu_4N^+), have been synthesized and fully characterized. These tris-chelate complexes can have two unique geometrical forms, synclastic and anticlastic, due to the unsymmetric nature of the ndt ligand in the direction perpendicular to the MS_2 coordination plane, and existence of such isomers has been established by the X-ray derived structures of [Ph_4P][Ta(ndt)$_3$] (**2a**) (synclastic) and [Et_4N][Nb(ndt)$_3$] (**1b**) (anticlastic). According to the IR spectra, the geometrical preference in solid was found to be governed by the size of countercations but not by the choice of metal, Nb or Ta. When the cation is similar in size to [M(ndt)$_3$]$^-$, e.g., Ph_4P^+ and *n*-Bu_4N^+, the synclastic configuration is preferred, while with the small Et_4N^+ cation, the alternative anticlastic configuration becomes feasible. The variable-temperature ^1H NMR study reveals that the two isomers coexist in solution (CD_2Cl_2) with a nearly statistical distribution, indicating that their relative stability is well-balanced. Activation parameters of the synclastic $\rightleftarrows$ anticlastic interconversion suggest non-bond-rupture pathways: **1b**, $\Delta H^\ddagger$ = 9.2 ± 0.5 kcal/mol, $\Delta S^\ddagger$ = −11.5 ± 1.8 eu; **2a**, $\Delta H^\ddagger$ = 11.1 ± 0.5 kcal/mol, $\Delta S^\ddagger$ = −8.8 ± 1.8 eu. In the synclastic structure of **2a**, the TaS_6 core adopts a geometry in between the octahedral and trigonal-prismatic limits. On the other hand, the NbS_6 core in anticlastic **1b** distorts toward a bicapped tetrahedron (BCT), which provides the first well-characterized example of d^0 six-coordinate complexes showing a distinct BCT geometry. The nature of M–S bonds in these distorted structures is examined by extended Hückel MO calculations. Crystal data: **2a** solvated by CH_3CN, monoclinic space group $P2_1/c$ with a = 18.061 (4) Å, b = 15.406 (4) Å, c = 18.400 (5) Å, β = 117.07 (2)°, Z = 4, R = 0.073 for 3305 independent reflections; **1b**, monoclinic space group Cc with a = 17.489 (3) Å, b = 11.040 (2) Å, c = 17.573 (4) Å, β = 107.37 (2)°, Z = 4, R = 0.041 for 3097 independent reflections.

While the majority of six-coordinate transition-metal complexes assume an octahedral (OH) structure (A), substantial departures

A B C

from this polyhedral paragon are also established. Two principal types of nonoctahedral geometries have emerged: one is a trigonal prism (TP) (B), and the other is distortion toward a bicapped tetrahedron (BCT) (C).[1] The former structure and those lying between the two limiting geometries, TP and OH (or antiprism), have occasionally been observed in d^0–d^2 complexes with chelating ligands[2] and in several metal sulfides and selenides.[3] Still rare is the latter C_{2v} distortion of the octahedron as exemplified by d^6 metal dihydrides of the general formula H_2ML_4[4] and by a few d^4 six-coordinate complexes, e.g., Mo(*t*-BuO)$_2$(CO)$_2$(py)$_2$,[5] $MoBr_2(CO)_2(PPh_3)_2$,[6] $Mo(CO)_2[S_2CN(i\text{-}Pr)_2]_2$,[7] and Mo(*t*-BuS)$_2$(*t*-BuNC)$_4$.[8]

On the other hand, a recent theoretical study on the hypothetical d^0 compound TiR_6^{2-} (R = H, CH_3) has demonstrated that in the optimized structure the molecule is deformed considerably toward BCT and that there is a good electronic reason behind such distortion.[9] However, the experimentally observed mode of deformation in d^0 ML_6, when it occurs, has so far been limited to a trigonally twisted octahedron leading to TP or near TP, except for the epoch-making structures of $TiCl_3R(Me_2PCH_2CH_2PMe_2)$ (R = CH_3, C_2H_5).[10] In these alkyl complexes, the presence of the agostic interaction between Ti and C–H bonds accompanies opening up of the R–Ti–Cl angles in an "equatorial" plane, while the "axial" Cl–Ti–Cl spine remains linear. Thus no authenticated example of BCT d^0 ML_6 has yet been reported.

† Department of Macromolecular Science.
‡ Department of Applied Chemistry.

(1) (a) Eisenberg, R. *Prog. Inorg. Chem.* **1970**, *12*, 295–369. (b) Wentworth, R. A. D. *Coord. Chem. Rev.* **1972**, *9*, 171–187. (c) Hoffmann, R.; Howell, J. M.; Rossi, A. R. *J. Am. Chem. Soc.* **1976**, *98*, 2484–2492, and references therein. (d) Burdett, J. K. *Inorg. Chem.* **1976**, *15*, 212–219. (e) Kepert, D. L. *Inorganic Stereochemistry*; Springer-Verlag: Berlin, 1982.

(2) (a) Eisenberg, R.; Ibers, J. A. *J. Am. Chem. Soc.* **1965**, *87*, 3776–3778. (b) Smith, A. E.; Schrauzer, G. N.; Mayweg, V. P.; Heinrich, W. *J. Am. Chem. Soc.* **1965**, *87*, 5798–5799. (c) Brown, G.; Stiefel, E. I. *Inorg. Chem.* **1973**, *12*, 2140–2147. (d) Martin, J. L.; Takats, J. *Inorg. Chem.* **1975**, *14*, 1358–1364. (e) Cowie, M.; Bennett, M. J. *Inorg. Chem.* **1976**, *15*, 1589–1603. (f) Yamanouchi, K.; Enemark, J. H. *Inorg. Chem.* **1978**, *17*, 2911–2917. (g) Draganjac, M.; Coucouvanis, D. *J. Am. Chem. Soc.* **1983**, *105*, 139–335. (h) Comba, P.; Sargeson, A. M.; Engelhardt, L. M.; Harrowfield, J. MacB.; White, A. H.; Horn, E.; Snow, M. R. *Inorg. Chem.* **1985**, *24*, 2325–2327. (i) Boyde, S.; Garner, D.; Enemark, J. H.; Bruck, M. A.; Kristofzski, J. G. *J. Chem. Soc., Dalton Trans.* **1987**, 2267–2271. (j) Colmanet, S. F.; Williams, G. A.; Mackay, M. F. *J. Chem. Soc., Dalton Trans.* **1987**, 2305–2310. (k) Diamantis, A. L.; Manikas, M.; Salam, M. A.; Snow, M. R.; Tiekink, E. R. T. *Aust. J. Chem.* **1988**, *41*, 453–468.

(3) (a) Wilson, J. A.; Yoffe, A. D. *Adv. Phys.* **1969**, *18*, 193–335. (b) Hulliger, F. *Struct. Bonding* **1968**, *4*, 83–181. *Crystallography and Crystal Chemistry of Materials with Layered Structures*; Levy, F., Ed.; Reidel: Boston, 1976. (c) Kertesz, M.; Hoffmann, R. *J. Am. Chem. Soc.* **1984**, *106*, 3453–3460.

(4) (a) Tebbe, F. N.; Meakin, P.; Jesson, J. P.; Mutterties, E. L. *J. Am. Chem. Soc.* **1970**, *92*, 1068–1070. (b) Guggenberger, L. J.; Titus, D. D.; Flood, M. T.; Marsh, R. E.; Orio, A. A.; Gray, H. B. *J. Am. Chem. Soc.* **1972**, *94*, 1135–1143.

(5) Chisholm, M. H.; Huffman, J. C.; Kelly, R. L. *J. Am. Chem. Soc.* **1979**, *101*, 7615–7617.

(6) Drew, M. G. B.; Tomkins, I. B.; Colton, R. *Aust. J. Chem.* **1970**, *23*, 2517–2570.

(7) Templeton, J. L.; Ward, B. C. *J. Am. Chem. Soc.* **1980**, *102*, 6568–6569.

(8) Kamata, M.; Hirotsu, K.; Higuchi, T.; Tatsumi, K.; Hoffmann, R.; Yoshida, T.; Otsuka, S. *J. Am. Chem. Soc.* **1981**, *103*, 5772–5778.

(9) (a) Demalliens, A.; Jean, Y.; Eisenstein, O. *Organometallics* **1986**, *5*, 1457–1464. (b) Eisenstein, O.; Jean, Y. *J. Am. Chem. Soc.* **1985**, *107*, 1177–1186.

0002-7863/89/1511-7766$01.50/0

In the course of our study on chemistry of homoleptic alkanedithiolate complexes of group 5 metals,[11] we have introduced the norbornane-*exo*-2,3-dithiolate (ndt) ligand,[12] where chelation to transition-metal systems is hitherto unknown. This paper describes syntheses and structures of $[A][M(ndt)_3]$ (A = Et_4N, *n*-Bu_4N, Ph_4P; M = Nb(V), Ta(V)). These complexes exhibit two interesting structural features. One has something to do with a unique aspect of the ndt ligand in that the bicyclo[2.2.1]alkane portion generates an unsymmetric environment in the direction perpendicular to the MS_2 coordination plane. Therefore, the tris-chelate complexes derived from the ndt ligand can exist in two geometrically isomeric forms, synclastic (D) and anticlastic (E),[13] each of which could be enantiomeric in case no mirror

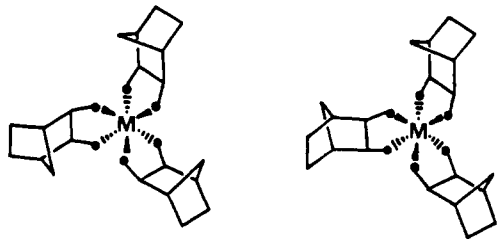

Synclastic Anticlastic

D E

symmetry bisecting three ndt ligands is imposed. In fact, we were successful in isolating complex salts consisting of either synclastic or anticlastic $[M(ndt)_3]^-$ (M = Nb, Ta) anions and found that the countercation controlled the geometrical preference in the solid, where the crystal structures of synclastic $[Ph_4P][Ta(ndt)_3]$ (**2a**) and anticlastic $[Et_4N][Nb(ndt)_3]$ (**1b**) were examined by X-ray analysis. On the other hand, a variable-temperature ^1H NMR study in CD_2Cl_2 indicates that the two isomers coexist in solution regardless of the countercation and that they undergo facile interconversion.

Another point of interest is that the MS_6 coordination geometries of both **1b** and **2a** deviate from an ideal octahedron and that they do so in quite different ways. For the synclastic complex, **2a**, the familiar trigonal-twist deformation is perturbed by nonequivalence of the two Ta–S bonds to each ndt chelate, which results in the three short and three long Ta–S distances belonging to opposite triangular faces of sulfur atoms. In contrast, the anticlastic complex, **1b**, favors distortion toward BCT, which provides the first well-characterized example of a d^0 six-coordinate complex, to our knowledge, having a distinct BCT structure. With this detailed structural information and the variable-temperature NMR spectra in hand, we explore a possible fluxional behavior in the class of d^0 tris-chelate structures. In addition, we discuss the nature of the M–S bonds under these two deformed coordination environments, with the aid of extended Hückel calculations.

Experimental Section

General Details. All experiments except for part of the ligand syntheses were performed under an argon atmosphere using standard Schlenk techniques. Reagent-grade acetonitrile and ether were distilled from calcium hydride and benzophenone ketyl, respectively, under argon. Dimethylformamide was distilled from benzene–azeotrope and then from barium oxide under argon. All deuteriated NMR solvents were dried by trap-to-trap distillation from calcium hydride.

Bicyclo[2.2.1]hepta-*exo-cis*-2,3-dithiol (H_2ndt) was prepared from bicyclo[2.2.1]hepta-2-ene and elemental sulfur, via *exo*-3,4,5-trithiatricyclo[5.2.1.$0^{2,6}$]decane, as described in the literature.[12b] Li_2ndt was prepared by adding butyllithium to H_2ndt in diethyl ether and isolated straightforwardly as a white powder. $[Ph_4P][M(SCH_2CH_2S)_3]$ and $[Et_4N][M(SCH_2CH_2S)_3]$ (M = Nb, Ta) were prepared by treating MCl_5 with $Li_2(SCH_2CH_2S)$ and Ph_4PBr (or Et_4NCl) according to the method we reported previously.[11b,d] $[n\text{-}Bu_4N][Nb(SCH_2CH_2S)_3]$ was synthesized in a similar manner using *n*-Bu_4NCl.

^1H NMR spectra were recorded on Varian XL-100 and JEOL GX-400 spectrometers. NMR data are listed in ppm downfield from TMS, while coupling constants are quoted in hertz. ^{13}C NMR were obtained at 22.6 MHz using a JEOL FX-90 spectrometer. Infrared spectra were recorded on Jasco DS-402G and Hitachi FIS-3 spectrometers, while Raman spectra were measured on a Jasco R-800 spectrometer equipped with a He–Ne laser, NEC GLG 5800. For UV–visible spectra, a Jasco UVIDEC-5A spectrometer was used. Electrochemical measurements were performed with standard instrumentation Yanaco P8-CV, using a Pt working electrode, DMF solvent, and 0.1 M (*n*-Bu_4N)(ClO_4) supporting electrolyte.

Preparation of Compounds. $[Ph_4P][Nb(ndt)_3]\cdot CH_3CN$ (1a). Method I. An acetonitrile solution (20 mL) of $NbCl_5$ (0.8 g, 2.9 mmol) was added to a mixture of Li_2ndt (1.8 g, 9.5 mmol) and Ph_4PBr (1.1 g, 2.6 mmol) in acetonitrile (15 mL) at 0 °C. The reaction mixture was allowed to warm to room temperature and stirred at this temperature for 1 h. As the product formed, the solution turned dark green and a white precipitate (LiCl and LiBr) was observed. The solution was concentrated in vacuo to ca. 20 mL, and insoluble whitish materials were filtered off. A greenish black spectroscopically pure powder of **1a** was precipitated from the filtrate upon standing at −20 °C overnight (1.6 g, 57% yield). Subsequent recrystallization from acetonitrile gave analytically pure dark green crystals.

Method II. To a DMF (50 mL) solution of $[Ph_4P][Nb(SCH_2CH_2S)_3]$ (1.9 g, 2.5 mmol) was added an excess amount of H_2ndt (3.8 g, 23.7 mmol). The solution was stirred for ca. 4 h at 60 °C, during which time the color changed from dark red to dark green. The solvent was removed in vacuo, and the resultant residue was washed with ether (20 mL × 4) and then recrystallized from acetonitrile to yield dark green crystals of **1a** (2.0 g, 80%). Mp: 149–157 °C dec. ^1H NMR (400 MHz, CD_2Cl_2; 100 MHz, CD_3CN) and ^{13}C NMR (22.6 MHz, DMF-d_7): data are given in Table IV, with the numbering scheme adopted. Far-IR (Nujol mull): ν_{max} 393 (s), 370 (s), 346 (m), 321 (s), 260 (w), 232 (m) cm^{-1}. Raman (crystals): ν_{max} 395 (s), 372 (w), 337 (s) cm^{-1}. UV–visible (DMF): λ_{max} ($\epsilon_{max} \times 10^{-4}$, M^{-1} cm^{-1}) 578 (0.26), 397 (0.71), 361 (0.78) nm. CV (DMF, (*n*-Bu_4N)(ClO_4) electrolyte): $E_{1/2}$ (vs SCE) −1.15 V [Nb(V)/Nb(IV)]. Anal. Calcd for $C_{47}H_{53}NPS_6Nb$: C, 59.53; H, 5.63; N, 1.48; S, 20.29. Found: C, 59.31; H, 5.74; N, 1.49; S, 19.99.

$[Et_4N][Nb(ndt)_3]$ (1b). The reaction system $NbCl_5$ (0.9 g, 3.3 mmol), Li_2ndt (2.0 g, 12 mmol), and Et_4NCl (0.5 g, 3 mmol) in acetonitrile (Method I) afforded a crude product of **1b** as brownish green powder (1.1 g, 48%), and recrystallization from acetonitrile gave dark green crystals. Analytically pure dark green crystals of **1b** were synthesized more conveniently by reaction of $[Et_4N][Nb(SCH_2CH_2S)_3]$ (0.44 g, 0.88 mmol) with excess H_2ndt (1.5 g, 11 mmol) in DMF (Method II) (0.50 g, 82%). Mp: 214–217 °C dec. ^1H NMR (100 MHz, CD_3CN): δ 4.09 (d, J_{H1H6} = 2, 6 H, ndt H1), 3.19 (q, J_{HH} = 7, 8 H, NCH_2CH_2), 2.46 (dt, J_{H5H6} = 9, J_{H3H5} = 2, 3 H, ndt H5), 2.20 (m, 6 H, ndt H2), 1.14–1.62 (m, 12 H, ndt H3, H4), 1.23 (tt, J_{HH} = 7, 12 H, NCH_2CH_3), 1.02 (dt, J_{H1H6} = 2, J_{H5H6} = 9, 3 H, ndt H6). Far-IR (Nujol mull): ν_{max} 407 (s), 388 (s), 381 (s), 370 (s), 345 (s), 326 (s), 234 (m), 210 (m) cm^{-1}. Raman (crystals): ν_{max} 395 (m), 327 (w), 337 (s) cm^{-1}. UV–visible (DMF): λ_{max} ($\epsilon_{max} \times 10^{-4}$, M^{-1} cm^{-1}) 577 (0.31), 395 (0.87), 360 (0.96), 281 (0.80) nm. CV (DMF): $E_{1/2}$ (vs SCE) −1.15 V [Nb(V)/Nb(IV)]. Anal. Calcd for $C_{29}H_{50}NS_6Nb$: C, 49.90; H, 7.22; N, 2.01; S, 27.56; Nb, 13.31. Found: C, 49.89; H, 7.29; N, 2.13; S, 27.35; Nb, 13.39.

$[n\text{-}Bu_4N][Nb(ndt)_3]$ (1c). Reaction of $[n\text{-}Bu_4N][Nb(SCH_2CH_2S)_3]$ (2.0 g, 3.3 mmol) with H_2ndt (3.2 g, 20 mmol) in DMF at 60 °C, followed by recrystallization from acetonitrile (Method II), yielded **1c**

(10) (a) Dawoodi, Z.; Green, M. L. H.; Mtetwa, V. S. B.; Prout, K. *J. Chem. Soc., Chem. Commun.* **1982**, 802–803, 1410–1411. (b) Dawoodi, Z.; Green, M. L. H.; Mtetwa, V. S. B.; Prout, K.; Schultz, A. J.; Williams, J. M.; Koetzle, T. F. J. *J. Chem. Soc., Dalton Trans.* **1986**, 1629–1637.

(11) (a) Tatsumi, K.; Takeda, J.; Sekiguchi, Y.; Kohsaka, M.; Nakamura, A. *Angew. Chem.* **1985**, *97*, 355–356; *Angew. Chem., Int. Ed. Engl.* **1985**, *24*, 332–333. (b) Tatsumi, K.; Sekiguchi, Y.; Nakamura, A.; Cramer, R. E.; Rupp, J. J. *Angew. Chem.* **1986**, *98*, 95–96; *Angew. Chem., Int. Ed. Engl.* **1986**, *25*, 86–87. (c) Tatsumi, K.; Sekiguchi, Y.; Nakamura, A.; Cramer, R. E.; Rupp, J. J. *J. Am. Chem. Soc.* **1986**, *108*, 1358–1359. (d) Tatsumi, K.; Matsubara, I.; Sekiguchi, Y.; Nakamura, A.; Mealli, C. *Inorg. Chem.* **1989**, *28*, 773–780. (e) Tatsumi, K.; Sekiguchi, Y.; Sebata, M.; Nakamura, A.; Cramer, R. E.; Chung, T. *Angew. Chem.* **1989**, *101*, 83–85; *Angew. Chem., Int. Ed. Engl.* **1989**, *28*, 98–100.

(12) (a) Bicyclo[2.2.1]hepta-exo-cis-2,3-dithiolate. (b) Shields, T. C.; Kurtz, A. N. *J. Am. Chem. Soc.* **1969**, *91*, 5415–5416.

(13) With ndt chelates in the $M(L\text{–}L)_3$ type complexes, there emerge two unique configurations that are imposed by relative orientation of a methene bridge of the bicyclo[2.2.1]alkane portion, being "bent" in the direction perpendicular to the MS_2 coordination plane. The ubiquitous cis–trans or endo–exo terminology is not appropriate for describing these isomeric structures. We here propose the terms "synclastic" and "anticlastic" to mean that the methene bridge of each ndt leans toward the same (and opposite) direction, respectively, in the periphery of the coordination sphere. These terms may be conveniently used for differentiating possible geometrical isomers of $M(L\text{–}L)_n$ (n = 2–4, etc.) complexes in general, in the case that the L–L chelate possesses a side-chain bending unsymmetrically with respect to the coordination plane.

as dark green crystals (2.0 g, 75%). Mp: 203–205 °C dec. ^{1}H NMR (100 MHz, CD_3CN): δ 4.06 (d, J_{H1H6} = 2, 6 H, ndt H1), 3.09 (t, J_{HH} = 8, 8 H, $NCH_2CH_2CH_2CH_3$), 2.41 (dt, J_{H5H6} = 10, J_{H3H5} = 2, 3 H, ndt H5), 2.16 (m, 6 H, ndt, H2), 0.84–1.72 (m, 43 H, ndt H3, H4, H6, $NCH_2CH_2CH_2CH_3$). Far-IR (Nujol mull): ν_{max} 400 (m), 386 (s), 369 (s), 340 (s), 324 (s), 316 (s), 260 (w), 222 (m) cm^{-1}. UV-visible (DMF): λ_{max} (ϵ_{max} × 10^{-4}, M^{-1} cm^{-1}) 577 (0.32), 396 (0.91), 359 (1.00), 282 (0.87) nm. Anal. Calcd for $C_{37}H_{66}NS_6Nb$: C, 54.85; H, 8.21; N, 1.73; S, 23.75. Found: C, 54.82; H, 8.26; N, 1.76; S, 22.80.

[Ph$_4$P][Ta(ndt)$_3$]·CH$_3$CN (2a). The preparation of this tantalum compound was very similar to that of the Nb analogue **1a**. The reaction system $TaCl_5$ (3.0 g, 8.4 mmol), Li_2ndt (4.3 g, 25 mmol), and Ph_4PBr (2.8 g, 6.7 mmol) in acetonitrile (Method I) gave **2a** as red powder (5.6 g, 62%), and recrystallization from acetonitrile yielded analytically pure red crystals. On the other hand, reaction of $[Ph_4P][Ta(SCH_2CH_2S)_3]$ (2.2 g, 2.5 mmol, orange color) with H_2ndt (3.8 g, 23.7 mmol) in DMF followed by recrystallization from acetonitrile (Method II) yielded **2a** as red crystals (1.9 g, 72%). Mp: 178–179 °C dec. ^{1}H NMR (400 MHz, CD_2Cl_2; 100 MHz, CD_3CN) and ^{13}C NMR (22.6 MHz, DMF-d_7): data are given in Table IV. Far-IR (Nujol mull): ν_{max} 386 (s), 360 (s), 350 (m), 320 (s), 247 (w), 223 (m) cm^{-1}. Raman (crystals): ν_{max} 399 (s), 390 (m), 361 (s), 350 (s), 343 (s), 192 (m), 162 (m), 130 (m) cm^{-1}. UV-visible (DMF): λ_{max} (ϵ_{max} × 10^{-4}, M^{-1} cm^{-1}) 494 (0.15), 322 (0.51) nm. CV (DMF): $E_{1/2}$ (vs SCE) −1.51 V [Ta(V)/Ta(IV)]. Anal. Calcd for $C_{47}H_{53}NPS_6Ta$: C, 54.48; H, 5.16; N, 1.35; S, 18.57. Found: C, 54.20, H, 5.20; N, 1.34; S, 18.59.

[Et$_4$N][Ta(ndt)$_3$] (2b). The reaction of $[Et_4N][Ta(SCH_2CH_2S)_3]$ (0.47 g, 0.80 mmol) with H_2ndt (1.3 g, 8.0 mmol) in DMF followed by recrystallization from acetonitrile (Method II) gave **2b** as red crystals (0.48 g, 76%). Mp: 231–234 °C dec. ^{1}H NMR (100 MHz, CD_3CN): δ 4.08 (d, J_{H1H6} = 2, 6 H, ndt H1), 3.20 (q, J_{HH} = 7, 8 H, NCH_2CH_3), 2.51 (dt, J_{H5H6} = 9, J_{H3H5} = 2, 3 H, ndt H5), 2.16 (m, 6 H, ndt H2), 1.12–1.56 (m, 12 H, ndt H3, H4), 1.23 (tt, J_{HH} = 7, 12 H, NCH_2CH_3), 1.05 (dt, J_{H1H6} = 2, J_{H5H6} = 9, 3 H, ndt H6). Far-IR (Nujol mull): ν_{max} 386 (s), 372 (s), 363 (s), 344 (s), 322 (s), 224 (m), 203 (m) cm^{-1}. Raman (crystals): ν_{max} 390 (m), 320 (w). UV-visible (DMF): λ_{max} (ϵ_{max} × 10^{-4}, M^{-1} cm^{-1}) 495 (0.32), 324 (1.1). CV (DMF): $E_{1/2}$ (vs SCE) −1.51 V [Ta(V)/Ta(IV)]. Anal. Calcd for $C_{29}H_{50}NS_6Ta$: C, 44.36; H, 6.35; N, 1.78; S, 24.48; Ta, 23.02. Found: C, 44.31; H, 6.41; N, 1.85; S, 24.42; Ta, 23.49.

X-ray Diffraction Study of [Et$_4$N][Nb(ndt)$_3$] (1b) and [Ph$_4$P][Ta(ndt)$_3$]·CH$_3$CN (2a). Crystals of **1b** and **2a** were sealed in thin-walled glass capillaries under argon. The reflection data were collected by the θ–2θ scan technique on a Rigaku automated four-circle diffractometer using graphite monochromated Mo Kα radiation (λ = 0.71069 Å). The accurate unit cell dimensions were determined by a least-squares fit of 2θ values of 25 centered reflections. Details of crystal data and other relevant information are summarized in Table I. The quality of each crystal was established by diffraction profiles examined by the ω-scan of several strong reflections. Three or four standard reflections were recorded at regular intervals to monitor the stability and orientation of the crystals, and they showed no significant decay throughout the data collection of the two complexes. The intensity measurements were corrected for Lorentz and polarization effects, while no absorption corrections were applied.

The structures were solved by the standard heavy-atom method using the UNICS-Osaka[14] and the SHELX-76[15] packages, which revealed the positions of Nb (**1b**) and Ta (**2a**) atoms unequivocally. The remaining non-hydrogen atoms were easily found in succeeding difference Fourier syntheses. Both structures were refined by the block-diagonal least-squares procedure where the function minimized was $\sum w(|F_o| - |F_c|)^2$. All the hydrogen atoms except for those of CH_3CN in **2a** were located on difference Fourier maps after anisotropic refinements of the non-hydrogen positions and were included in structure factor calculations in further refinement cycles. The weighting scheme is $w = (\sigma_{cs}^2 + a|F_o| + b|F_o|^2)^{-1}$, where σ_{cs} stands for the standard deviation obtained from the counting statistics and a and b are variables adjusted during the refinement cycles. The details of the refinements with the final R and R_w values are also given in Table I. The atomic scattering factors were taken from *International Tables for X-Ray Crystallography*.[16] The final atomic positional parameters of all non-hydrogen atoms for **1b** and **2a** are listed in Table II along with the equivalent isotropic thermal parameters B_{eq}.[17] Additional crystallographic data are available as supplementary material that include tables of anisotropic temperature factors, atomic parameters for hydrogen atoms, complete lists of bond distances and angles, and observed and calculated structure factors.

Table I. Crystal Data, Data Collection Parameters, and Refinement Details for $[Ph_4P][Ta(ndt)_3]$ (**2a**) and $[Et_4N][Nb(ndt)_3]$ (**1b**)

	2a	**1b**
formula		
cation	$C_{24}H_{20}P$	$C_8H_{20}N$
anion	$C_{21}H_{30}S_6Ta$	$C_{21}H_{30}S_6Nb$
solvent	C_2H_3N	
MW	1036.2	698.0
cryst syst	monoclinic	monoclinic
space gp	$P2_1/c$	Cc
a, Å	18.061 (4)	17.489 (3)
b, Å	15.406 (4)	11.042 (2)
c, Å	18.400 (5)	17.573 (4)
β, deg	117.07 (2)	107.37 (2)
U, Å^3	4558.9 (19)	3238.4 (11)
D_{calcd}, g cm^{-3}	1.510	1.432
Z	4	4
$F(000)$	2104	1472
μ (Mo Kα), cm^{-1}	28.8	7.54
cryst size, mm	0.15 × 0.40 × 0.45	0.25 × 0.30 × 0.30
scan mode	θ–2θ	θ–2θ
scan width in 2θ, deg	1.6 + 0.70 tan θ	1.8 + 0.70 tan θ
scan speed in 2θ, deg min^{-1}	4	4
bckgd intens, s	5	5
2θ max, deg	42.0	54.0
no. reflcns colld	5332	3836
no. independent reflcns	4891	3530
R_{int}	0.037	0.024
no. of reflcns ($\|F_o\| > 3\sigma(F_o)$)	3305	3097
no. of atoms refined	56	37
no. of param refined	506	335
S (value of the error of fit)	1.12	1.15
weighting param (see text)		
a	0.0250	0.0180
b	0.0002	0.0004
final R value[a]	0.073	0.041
final R_w value[b]	0.078	0.044
Δ/σ[c]	0.06	0.02

[a] $R = \sum||F_o| - |F_c||/\sum|F_o|$. [b] $R_w = \{\sum w(|F_o| - |F_c|)^2/\sum w|F_o|^2\}^{1/2}$. [c] Maximum shift to esd ratio for non-hydrogen atoms.

Molecular Orbital Calculations. All calculations were carried out with the extended Hückel method[18] utilizing the modified Wolfsberg–Helmholz formula.[19] We determined the valence-state ionization potentials, H_{ii}, of Ta orbitals by charge-iterative calculations on $[Ta(SCH_2CH_2S)_3]^-$ (θ = 16°; Chart I), assuming a quadratic charge dependence of H_{ii}. This is very similar to the way in which the Nb parameters were determined in our previous paper.[11d] The metal orbital exponents were taken from other work.[20] Table III summarizes these metal parameters as well as the standard S, C, and H parameters used for these calculations.

In the comparative calculations on $[Nb(ndt)_3]^-$ and $[Ta(ndt)_3]^-$, the metal to sulfur distances were fixed at 2.43 Å. Also fixed was the S–M–S chelate angle of 82°. For the ndt ligand, the S–C lengths were set at 1.82 Å, with all the C–C and C–H distances being set at 1.50 and 1.09 Å, respectively. The C2–C1–C3 angle is 103°, and the dihedral angles defined between S–C1–C2–S and C1–C2–C3–C6 planes and between C1–C2–C3–C6 and C3–C4–C5–C6 planes were assumed to be 120°; the atom numbering scheme is shown below in F.

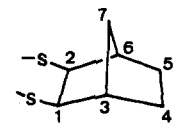

F

(14) Ashida, T. *UNICS-Osaka*: *The Universal Crystallographic Computing System-Osaka*, 2nd ed.; Yasuoka, N., Ed.; The Computer Center Osaka University: Osaka, Japan, 1979.

(15) Sheldrick, G. M. *SHELX-76*: *Program for Crystal Structure Determination*; University of Cambridge: Cambridge, England, 1976.

(16) *International Tables for X-Ray Crystallography*; Kynoch: Birmingham, England, 1974; Vol. IV.

(17) Hamilton, W. C. *Acta Crystallogr.* **1959**, *12*, 609–611.

(18) (a) Hoffmann, R. *J. Chem. Phys.* **1963**, *39*, 1397–1412. (b) Summerville, R.; Hoffmann, R. *J. Am. Chem. Soc.* **1976**, *98*, 7240–7254.

(19) Ammeter, J. H.; Bürgi, H.-B.; Thibeault, J. C.; Hoffmann, R. *J. Am. Chem. Soc.* **1978**, *100*, 3686–3692.

(20) (a) Basch, H.; Gray, H. B. *Theor. Chim. Acta* **1966**, *4*, 367–376. (b) Tatsumi, K.; Hoffmann, R. *J. Am. Chem. Soc.* **1981**, *103*, 3328–3341, and references therein.

Table II. Fractional Atomic Coordinates and Equivalent Isotropic Thermal Parameters of Non-Hydrogen Atoms in **2a** and **1b** with Esd's in Parentheses

atom	x	y	z	B_{eq},[a] Å²	atom	x	y	z	B_{eq},[a] Å²
(a) $[Ph_4P][Ta(ndt)_3]$ (**2a**)									
Ta	0.30237 (6)	0.31477 (6)	0.27810 (5)	3.8	P	0.9031 (4)	0.2809 (4)	0.9652 (4)	3.8
S(11)	0.3532 (4)	0.1749 (5)	0.2646 (5)	6.4	C(41)	0.9768 (11)	0.2582 (13)	0.9254 (12)	3.9
S(12)	0.1699 (4)	0.2389 (4)	0.2206 (4)	4.5	C(42)	1.0590 (13)	0.2575 (15)	0.9816 (13)	5.1
S(21)	0.3645 (4)	0.2836 (4)	0.4226 (4)	4.9	C(43)	1.1187 (14)	0.2384 (15)	0.9553 (14)	5.5
S(22)	0.2366 (4)	0.4299 (4)	0.3189 (3)	4.2	C(44)	1.0933 (16)	0.2210 (14)	0.8727 (15)	6.3
S(31)	0.4324 (4)	0.3753 (5)	0.2975 (4)	6.0	C(45)	1.0126 (17)	0.2215 (16)	0.8221 (14)	6.8
S(32)	0.2527 (4)	0.3859 (5)	0.1465 (4)	4.7	C(46)	0.9517 (14)	0.2398 (16)	0.8454 (13)	5.6
C(11)	0.2722 (17)	0.0923 (16)	0.2329 (17)	8.0	C(51)	0.8010 (12)	0.2934 (13)	0.8807 (12)	4.2
C(12)	0.1807 (14)	0.1251 (17)	0.2006 (15)	7.0	C(52)	0.7847 (13)	0.3544 (16)	0.8195 (13)	5.4
C(13)	0.1537 (17)	0.0681 (18)	0.2515 (18)	8.4	C(53)	0.7026 (15)	0.3632 (16)	0.7616 (13)	6.4
C(14)	0.1395 (16)	−0.0257 (16)	0.2237 (16)	7.6	C(54)	0.6430 (12)	0.3149 (17)	0.7634 (14)	6.7
C(15)	0.2275 (20)	−0.0540 (18)	0.2486 (21)	10.6	C(55)	0.6579 (15)	0.2525 (14)	0.8247 (15)	6.5
C(16)	0.2819 (14)	0.0259 (15)	0.2851 (21)	9.6	C(56)	0.7396 (14)	0.2434 (15)	0.8832 (14)	6.1
C(17)	0.2311 (16)	0.0621 (20)	0.3298 (16)	9.0	C(61)	0.9281 (11)	0.3775 (11)	1.0273 (10)	2.7
C(21)	0.3369 (13)	0.3627 (13)	0.4797 (12)	4.2	C(62)	1.0012 (14)	0.3818 (15)	1.1002 (13)	6.4
C(22)	0.2681 (12)	0.4325 (12)	0.4289 (11)	3.7	C(63)	1.0220 (15)	0.4586 (18)	1.1480 (14)	7.2
C(23)	0.3121 (13)	0.5181 (13)	0.4648 (12)	4.3	C(64)	0.9691 (15)	0.5246 (13)	1.1242 (12)	5.7
C(24)	0.3193 (14)	0.5242 (13)	0.5501 (14)	5.3	C(65)	0.8978 (15)	0.5203 (15)	1.0512 (13)	6.7
C(25)	0.3894 (15)	0.4600 (17)	0.6001 (13)	6.5	C(66)	0.8782 (14)	0.4485 (14)	1.0034 (14)	6.4
C(26)	0.4118 (12)	0.4212 (12)	0.5339 (12)	4.2	C(71)	0.9079 (12)	0.1911 (12)	1.0295 (11)	3.7
C(27)	0.4005 (12)	0.4974 (14)	0.4815 (13)	4.8	C(72)	0.9264 (14)	0.1113 (14)	1.0100 (12)	5.2
C(31)	0.4208 (16)	0.4414 (19)	0.2053 (14)	7.3	C(73)	0.9291 (13)	0.0373 (15)	1.0569 (14)	5.9
C(32)	0.3303 (15)	0.4375 (23)	0.1337 (13)	9.6	C(74)	0.9132 (14)	0.0457 (15)	1.1199 (15)	6.3
C(33)	0.3492 (15)	0.4001 (21)	0.0706 (13)	8.1	C(75)	0.8916 (13)	0.1267 (16)	1.1394 (12)	5.6
C(34)	0.3955 (16)	0.4593 (21)	0.0403 (15)	9.0	C(76)	0.8893 (13)	0.2003 (15)	1.0938 (12)	5.1
C(35)	0.4830 (16)	0.4644 (22)	0.1115 (16)	9.7	C(1S)	0.569 (2)	0.280 (3)	−0.013 (3)	13.0
C(36)	0.4764 (13)	0.4054 (18)	0.1739 (13)	6.4	C(2S)	0.651 (3)	0.281 (3)	0.033 (3)	15.0
C(37)	0.4176 (15)	0.3342 (16)	0.1187 (17)	7.6	N(1S)	0.721 (3)	0.293 (3)	0.078 (3)	18.0
(b) $[Et_4N][Nb(ndt)_3]$ (**1b**)									
Nb	1.0	−0.04268 (5)	0.5	2.6	C(26)	1.1804 (5)	0.2720 (7)	0.4951 (5)	3.8
S(11)	1.07542 (10)	−0.20042 (16)	0.59050 (11)	2.7	C(27)	1.1676 (5)	0.3218 (8)	0.5710 (5)	4.0
S(12)	0.90491 (12)	−0.08270 (18)	0.57264 (13)	3.5	C(31)	0.9301 (4)	−0.1824 (7)	0.3078 (4)	2.7
S(21)	1.13521 (10)	0.03497 (16)	0.51688 (11)	2.8	C(32)	0.8905 (4)	−0.0566 (6)	0.2931 (4)	2.6
S(22)	0.98794 (11)	0.16803 (16)	0.54536 (12)	2.9	C(33)	0.7998 (5)	−0.0867 (7)	0.2654 (5)	3.6
S(31)	0.98992 (10)	−0.21227 (15)	0.41062 (11)	2.6	C(34)	0.7791 (5)	−0.1334 (8)	0.1788 (5)	4.1
S(32)	0.91745 (10)	0.04539 (16)	0.37849 (10)	2.7	C(35)	0.8204 (5)	−0.2594 (8)	0.1908 (5)	3.8
C(11)	0.9982 (4)	−0.3041 (7)	0.6028 (4)	2.7	C(36)	0.8571 (5)	−0.2690 (6)	0.2823 (5)	3.2
C(12)	0.9141 (4)	−0.2465 (7)	0.5925 (5)	2.7	C(37)	0.7961 (5)	−0.2016 (8)	0.3121 (5)	3.8
C(13)	0.8994 (5)	−0.2748 (8)	0.6728 (5)	3.6	N	0.7263 (4)	0.3292 (5)	0.3589 (4)	2.9
C(14)	0.8821 (6)	−0.4084 (8)	0.6748 (6)	4.5	C(41)	0.7195 (4)	0.2306 (7)	0.2973 (5)	3.3
C(15)	0.9660 (7)	−0.4683 (7)	0.6856 (6)	4.6	C(42)	0.6380 (6)	0.1708 (9)	0.2697 (6)	5.2
C(16)	1.0202 (5)	−0.3570 (8)	0.6874 (5)	4.0	C(51)	0.8115 (5)	0.3744 (8)	0.3789 (5)	3.6
C(17)	0.9838 (6)	−0.2638 (9)	0.7307 (5)	4.4	C(52)	0.8356 (7)	0.4725 (9)	0.4429 (6)	5.8
C(21)	1.1109 (4)	0.1830 (6)	0.4679 (4)	2.7	C(61)	0.6652 (6)	0.4294 (8)	0.3272 (5)	4.1
C(22)	1.0413 (4)	0.2528 (6)	0.4877 (4)	2.7	C(62)	0.6692 (8)	0.4855 (10)	0.2501 (6)	6.1
C(23)	1.0830 (5)	0.3667 (7)	0.5302 (6)	3.9	C(71)	0.7090 (5)	0.2803 (7)	0.4334 (5)	3.1
C(24)	1.0982 (6)	0.4507 (8)	0.4665 (7)	5.0	C(72)	0.7644 (5)	0.1829 (8)	0.4752 (5)	4.3
C(25)	1.1635 (6)	0.3823 (8)	0.4401 (6)	4.8					

[a] As defined by Hamilton.[17]

Table III. Atomic Parameters Used for Extended Hückel Calculations

atom	orbital	H_{ii}, eV	exponent[a]
Ta	6s	−9.36	2.280
	6p	−6.23	2.241
	5d	−11.04	4.762 (0.6600) + 1.938 (0.5592)
Nb	5s	−9.41	1.90
	5p	−6.27	1.85
	4d	−11.10	4.08 (0.6401) + 1.64 (0.5516)
S	3s	−20.00	1.817
	3p	−13.30	1.817
C	2s	−21.40	1.625
	2p	−11.40	1.625
H	1s	−13.60	1.300

[a] The numbers in parentheses are contraction coefficients used in the double-ζ expansion.

Scheme I

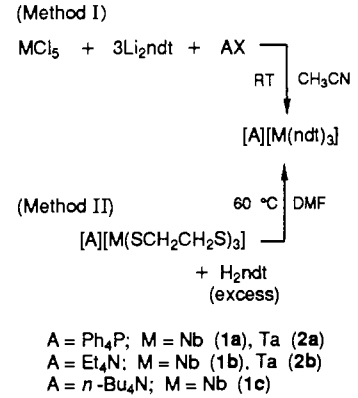

A = Ph_4P; M = Nb (**1a**), Ta (**2a**)
A = Et_4N; M = Nb (**1b**), Ta (**2b**)
A = n-Bu_4N; M = Nb (**1c**)

Results and Discussion

Synthesis and Characterization. Two methods were employed for the synthesis of a series of tris(norbornane-*exo*-2,3-dithiolate) complexes of Nb and Ta as shown in Scheme I. The first method is the direct reaction of MCl_5 (M = Nb, Ta) with 3 equiv of Li_2ndt and Ph_4PBr (or Et_4NCl) in acetonitrile. The compounds **1a**, **1b**, and **2a** were prepared as green (for Nb) or red (for Ta) powder (48–62% yield) by this method. Upon recrystallization from acetonitrile, analytically pure deep green (Nb) or red (Ta) crystals

Table IV. 400-MHz ^{1}H NMR and 22.6-MHz ^{13}C NMR Data of $[Ph_4P][Nb(ndt)_3]$ (**1a**), $[Ph_4P][Ta(ndt)_3]$ (**2a**), and H_2ndt

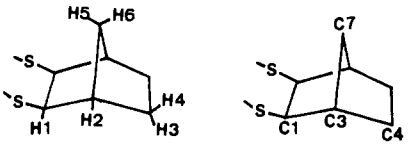

	chemical shift, ppm						coupling constant, Hz		
^{1}H NMR	H1	H2	H3	H4	H5	H6	J_{H1H6}	J_{H3H5}	J_{H5H6}
1a[a]	4.08 (d)	2.16 (m)	1.15 (m)	1.41 (m)	2.42 (d)	0.92 (dt)	1.7	(2)[d]	9.5
2a[a]	4.03 (s,br)	2.09 (m)	1.06 (m)	1.37 (m)	2.46 (s,br)	0.92 (d,br)	(2)[d]	(2)[d]	9.5
H_2ndt[b]	3.24 (m)	2.25 (m)	1.29 (m)	1.60 (m)	1.95 (dt)	1.18 (dt)	1.5	1.8	10.4

	chemical shift, ppm			
^{13}C NMR	C1	C3	C4	C7
1a[c]	71.3	49.3	28.8	34.1
2a[c]	69.5	49.9	29.0	32.7
H_2ndt[b]	(47.5, 47.1)		28.3	32.1

[a] Ppm downfield from TMS as a secondary standard, with CH_2Cl_2 as primary standard using the shift of CH_2Cl_2 relative to TMS as 5.28 ppm, 30 °C, in CD_2Cl_2. [b] Ppm downfield from TMS, RT, in $CDCl_3$. [c] RT, in DMF-d_7. [d] Estimated from the 100-MHz ^{1}H NMR, RT, in CD_3CN.

could be obtained. The second method involves a ligand exchange reaction of $[A][M(SCH_2CH_2S)_3]$ (A = Ph_4P, Et_4N, n-Bu_4N) in DMF at 60 °C with an excess amount of H_2ndt, which readily gave the desired products, **1a–c** and **2a,b**, as analytically pure crystals in 75–82% yields, after evaporation of the solvent and recrystallization of the residue from acetonitrile.

While neither of the two synthetic routes is very laborious, Method II is advantageous in that the ligand exchange proceeds cleanly and thereby affords pure crystalline products in high yields. In the case of Method I, relatively high solubility of Li_2ndt in acetonitrile appears to cause partial reduction of the metal in the reaction system, particularly for Nb(V), and the products $[A][Nb^V(ndt)_3]$ tend to be contaminated by some Nb(IV) species. Thus, careful air oxidation of the crude products is at times desirable for better yields. All the complexes, **1a–c** and **2a,b**, are diamagnetic and are mildly air/moisture sensitive. According to the elemental analyses and the ^{1}H NMR spectra, the Ph_4P^+ salts, **1a** and **2a**, were found to be solvated by acetonitrile.

The complexes $[A][M(ndt)_3]$ (**1**, **2**) exhibit temperature-dependent ^{1}H NMR spectra. The detailed analysis of their dynamic process will be given later in this paper, and we comment here on the principal features of the 30 °C 400-MHz ^{1}H NMR spectra and the room-temperature 22.6-MHz ^{13}C NMR spectra of $[Ph_4P][Nb(ndt)_3]$ (**1a**) and $[Ph_4P][Ta(ndt)_3]$ (**2a**), each of which is under a fast-exchange condition showing a single set of the ndt signals. The ndt proton/carbon resonances are summarized in Table IV, together with the H_2ndt data for comparison.

A well-isolated doublet at 4.08 ppm of **1a** can be assigned unambiguously to the H1 protons geminal to sulfur, where the splitting arises from the coupling with the H6 proton. The corresponding signal of **2a** is slightly broadened to become a singlet, while in its 100-MHz ^{1}H NMR spectrum, the peak splitting is discernible. We assigned the other proton signals with the aid of sequential decoupling procedures. Similar to the H1 resonance, these signals are somewhat broad for **2a**. For instance, the H5 resonance is so broad that even the sizable geminal coupling with H6 could not be seen. On the other hand, in the ^{13}C NMR spectra there appear a group of four singlets in the region expected for the ndt carbon atoms. The ^{1}H and ^{13}C NMR signals of **1a** and **2a** shift by varying degrees relative to those of metal-free H_2ndt. Most notable are large downfield shifts of the H1, H5, and C1 resonances upon coordination to the metal, while the C3 peak also moves to downfield moderately. These features are common to all the ndt complexes, **1a–c** and **2a,b**. For the closely related tris(alkanedithiolate) complexes of Nb and Ta, $[A][M(SCH_2CH_2S)_3]$ and $[A][M(SCH_2CH_2CH_2S)_3]$ (A = Ph_4P, Et_4N), we noticed a systematic downfield shift (albeit small, 0.2–0.4 ppm) of the ^{1}H NMR peaks associated with the methylene groups adjacent to sulfur, in going from Nb to Ta.[11d] Apparently this is not the case for the H1 resonances of the ndt complexes.

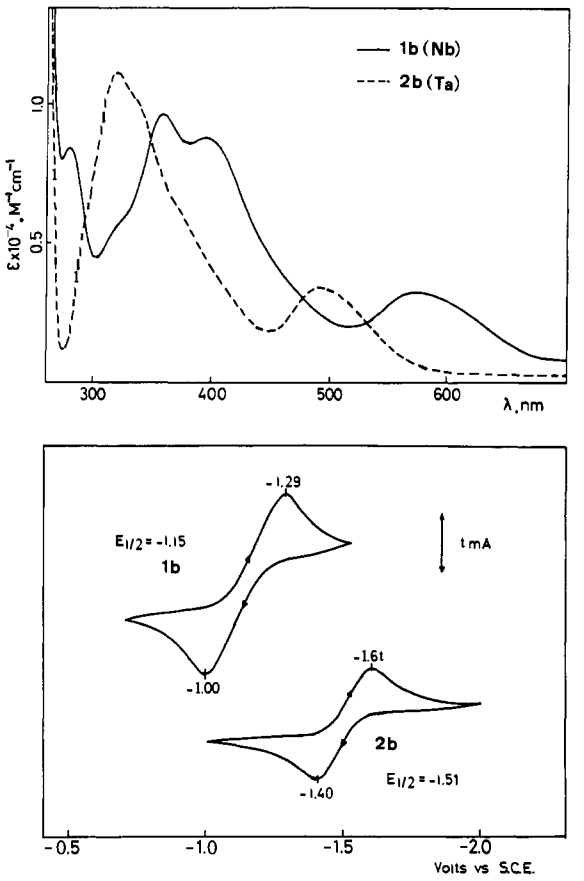

Figure 1. Electronic absorption (UV–vis) spectra (top) of $[Et_4N][Nb(ndt)_3]$ (**1b**) and $[Et_4N][Ta(ndt)_3]$ (**2b**) in DMF and their cyclic voltammograms (bottom) in DMF with (n-Bu_4N)(ClO_4) (0.1 M) as supporting electrolyte.

Figure 1 (top) shows the electronic spectra of $[Et_4N][M(ndt)_3]$ (M = Nb (**1b**), Ta (**2b**)) in DMF. The spectrum of **1b** features three low-energy absorption bands at 577 nm (band 1), 395 nm (band 2), and 360 nm (band 3) with shoulders at ca. 450 and 320 nm, all of which shift to lower wavelengths for the Ta analogue **2b**. As it ought to be, the identity of the countercation (Et_4N^+, n-Bu_4N^+, or Ph_4P^+) has a negligible effect on the spectral pattern. Because of their high intensities and a d^0 electron configuration of the metal, the observed absorptions can be attributed to sulfur-to-metal charge-transfer transitions. Interestingly, a change

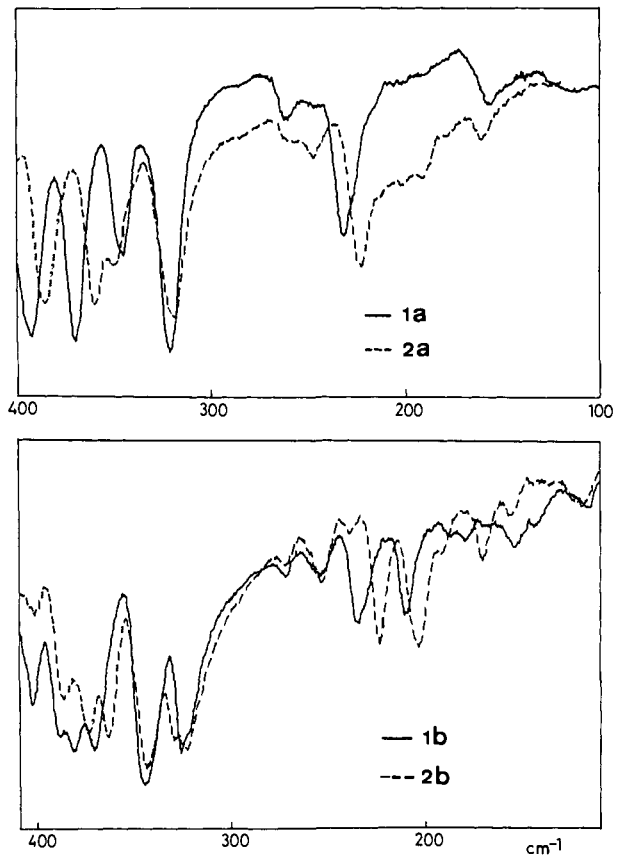

Figure 2. Comparison of the IR spectra in the 100–400-cm^{-1} region of $[Ph_4P][M(ndt)_3]$ (M = Nb (**1a**), Ta (**2a**)) (top) and $[Et_4N][M(ndt)_3]$ (M = Nb (**1b**), Ta (**2b**)) (bottom).

in the metal from Nb to Ta results in the nearly constant blue (hypsochromic) shift of these bands, viz., 0.35 eV (band 1), ~0.45 eV (band 2), 0.39 eV (band 3). It appears then that the vacant d level(s), into which the charge-transfer transitions occur, is of a similar type. An analogous nearly constant blue shift was found for the low-energy absorption bands of $[A][M(SCH_2CH_2S)_3]$ (M = Nb, Ta) and $[A][M(SCH_2CH_2CH_2S)_3]$, where the Nb to Ta shifts amount to 0.41–0.52 eV for the ethanedithiolate complexes and 0.46–0.48 eV for the propanedithiolate complexes.[11d]

Cyclic voltammetric measurements on **1a,b** and **2a,b** resulted in one reversible, well-behaved wave representing the Nb(V)/Nb(IV) and Ta(V)/Ta(IV) redox couples. Figure 1 (bottom) displays the voltammograms recorded for the Et_4N^+ salts along with their half-wave potentials, $E_{1/2}$ (vs SCE). As in the UV–visible spectra, the choice of the countercation, Et_4N^+ or Ph_4P^+, does not alter the main feature of the voltammograms in the range from −0.5 to −2.0 V. A comparison of the $E_{1/2}$ values for **1b** and **2b** shows that the replacement of Nb with Ta lowers $E_{1/2}$ by 0.36 V. The observed M(V)/M(IV) reduction potentials as well as the amount of the Nb to Ta negative shift are all close to those of $[M(SCH_2CH_2S)_3]^-$ (Nb, −1.20 V; Ta, −1.56 V) and $[M(SCH_2CH_2CH_2S)_3]^-$ (Nb, −1.25 V; Ta, −1.59 V), implying electronic similarity in solution among these tris(alkanedithiolate) complexes. The reduction process most likely involves an electron transfer to the lowest vacant metal d level of the "a_1" symmetry type.[1c,11d,21,22] Therefore, we interpret the observed Nb to Ta negative shift as a consequence of higher positioning of the Ta 5d energy level relative to Nb 4d. This diagnosis explains also the systematic blue shifts of the UV–visible absorption bands of **1a,b** and **2a,b**.

The far-IR study has provided us with interesting structural implications concerning the MS_6 coordination sphere. The spectra

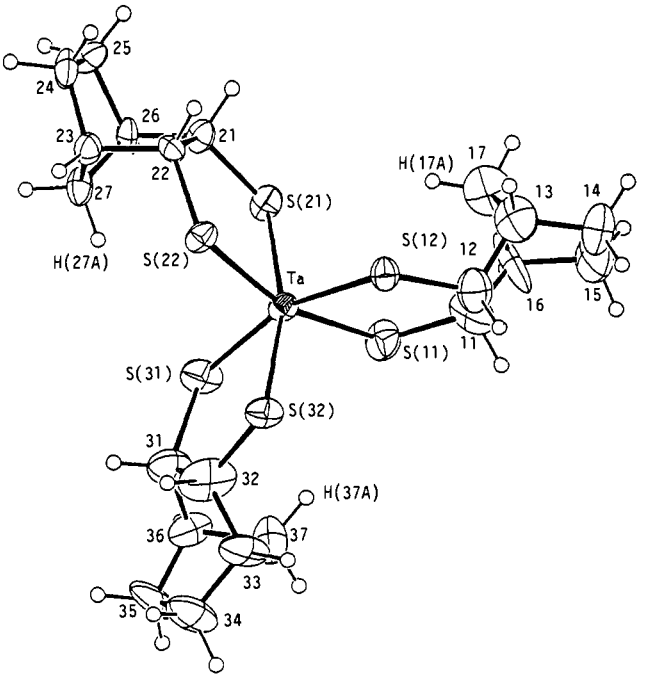

Figure 3. ORTEP view of the synclastic $[Ta(ndt)_3]^-$ anion of **2a** showing the atom-labeling scheme used in the tables. The thermal ellipsoids are drawn at the 50% probability level.

of **1a** and **2a** and **1b** and **2b** are superimposed in Figure 2 (top and bottom, respectively). We note two important aspects of the bands at 300–400 cm^{-1} arising from M–S stretching vibrations.[11d,23] One is the obvious difference in the spectral pattern between the Ph_4P^+ and Et_4N^+ salts implying that the MS_6 coordination geometry in the solid varies substantially depending on a choice of the countercation. On the other hand, a change in the metal from Nb to Ta does not alter the primal feature of the spectra, except that most of peaks shift to lower frequencies probably due to the mass effect. In the case of $[n\text{-}Bu_4N][Nb(ndt)_3]$ (**1c**), we obtained an IR spectrum very similar to those of the Ph_4P^+ salts, **1a** and **2a**.

The second, and actually more informative, aspect of the spectra has something to do with the number of intense peaks appearing at 300–400 cm^{-1}. According to the vibrational analysis based on a simplified MS_6 skeleton model, where chelation effects of the bidentate ligands are ignored and a coupling between M–S and S–C stretches are assumed to be small, normal modes for an ideal octahedron consist of A_{1g}, E_g, and T_{1u}, of which only T_{1u} is IR active. As the MS_6 unit twists from O_h to D_3 and to D_{3h} (trigonal distortion), the T_{1u} band splits into A_2 (A_2'') and E (E′), while E_g becomes IR active E (E′). The remaining A_{1g} band is kept IR inactive, correlating to A_1 (A_1').[24] Therefore, the IR spectrum of a trigonally deformed MS_6 is expected to show three peaks associated with M–S stretching vibrations, where A_2 and E derived from T_{1u} (O_h) would be more intense than the other E. As a matter of fact, we observed two strong IR peaks in the region 300–400 cm^{-1} for $[A][M(SCH_2CH_2S)_3]$, $[A][M(SCH_2CH_2CH_2S)_3]$, and $[A][M(SCH{=}CHS)_3]$ (A = Ph_4P,

(21) Green, J. C.; Kelly, M. R.; Grebenik, P. D.; Briant, C. E.; McEvoy, N. A.; Mingos, D. M. P. *J. Organomet. Chem.* **1982**, *228*, 239–247.

(22) Stiefel, E. I.; Eisenberg, R.; Rosenberg, R. C.; Gray, H. B. *J. Am. Chem. Soc.* **1966**, *88*, 2956–2966.

(23) The stretching frequencies of Nb=S and Ta=S bonds range from 487 to 552 cm^{-1} and from 474 to 516 cm^{-1}, respectively, while those in TaS_4^{3-} (424 cm^{-1}) and $Cp^*_2Ta_2S_6Li_4(THF)_4$ (434 cm^{-1}) are lower. See: (a) Drew, M. G. B.; Fowles, G. W. A.; Hobson, R. J.; Rice, D. A. *Inorg. Chim. Acta* **1976**, *20*, L35–L36. (b) Drew, M. G. B.; Rice, D. A.; Williams, D. M. *J. Chem. Soc., Dalton Trans.* **1983**, 2251–2256; **1984**, 845–848, 1087–1090; **1985**, 1821–1828. (c) Do, Y.; Simhon, E. D.; Holm, R. H. *Inorg. Chem.* **1983**, *22*, 3809–3812. (d) See ref 11c. (e) Müller, A.; Schmidt, K. H.; Tytko, K. H.; Bouwma, J.; Jellinek, F. *Spectrochim. Acta* **1972**, *A28*, 381–391. (f) Tatsumi, K.; Inoue, Y.; Nakamura, A.; Cramer, R. E.; VanDoorne, W.; Gilje, J. W. *J. Am. Chem. Soc.* **1989**, *111*, 782–783. (g) Tatsumi, K.; Sekiguchi, Y.; Kohsaka, M.; Sebata, M.; Nakamura, A.; Cramer, R. E.; Rupp, J. J., to be published.

(24) Nakamoto, K. *Infrared Spectra of Inorganic and Coordination Compounds*; Wiley: New York, 1970.

Table V. Selected Bond Distances (Å) and Bond Angles (deg) for $[Ph_4P][Ta(ndt)_3]$ (**2a**) and $[Et_4N][Nb(ndt)_3]$ (**1b**) with Esd's in Parentheses

	2a	1b		2a	1b
Ta/Nb-S(11)	2.398 (8)	2.460 (2)	S(21)-C(21)	1.82 (3)	1.837 (8)
Ta/Nb-S(12)	2.431 (7)	2.420 (3)	S(22)-C(22)	1.84 (3)	1.827 (8)
Ta/Nb-S(21)	2.418 (7)	2.449 (2)	S(31)-C(31)	1.91 (3)	1.827 (8)
Ta/Nb-S(22)	2.435 (6)	2.488 (3)	S(32)-C(32)	1.72 (4)	1.823 (8)
Ta/Nb-S(31)	2.398 (8)	2.416 (2)	P/N-C(41)	1.82 (3)	1.514 (10)
Ta/Nb-S(32)	2.427 (7)	2.398 (2)	P/N-C(51)	1.80 (3)	1.510 (11)
S(11)-C(11)	1.82 (4)	1.831 (8)	P/N-C(61)	1.80 (2)	1.524 (11)
S(12)-C(12)	1.82 (3)	1.839 (8)	P/N-C(71)	1.80 (3)	1.528 (10)
S(11)-Ta/Nb-S(12)	82.54 (24)	81.37 (7)	S(31)-Ta/Nb-S(32)	82.25 (24)	80.07 (7)
S(11)-Ta/Nb-S(21)	85.85 (25)	81.81 (7)	Ta/Nb-S(11)-C(11)	111.8 (11)	104.3 (3)
S(11)-Ta/Nb-S(22)	161.69 (24)	122.35 (7)	Ta/Nb-S(12)-C(12)	112.1 (9)	104.1 (3)
S(11)-Ta/Nb-S(31)	88.27 (26)	78.04 (7)	Ta/Nb-S(21)-C(21)	113.0 (8)	100.1 (3)
S(11)-Ta/Nb-S(32)	106.70 (25)	157.99 (7)	Ta/Nb-S(22)-C(22)	113.9 (7)	101.3 (3)
S(12)-Ta/Nb-S(21)	104.80 (22)	142.26 (8)	Ta/Nb-S(31)-C(31)	111.8 (10)	114.3 (3)
S(12)-Ta/Nb-S(22)	87.89 (21)	82.21 (8)	Ta/Nb-S(32)-C(32)	113.1 (13)	115.0 (3)
S(12)-Ta/Nb-S(31)	162.81 (24)	105.85 (7)	C(41)-P/N-C(51)	108.8 (10)	105.4 (6)
S(12)-Ta/Nb-S(32)	86.52 (21)	102.59 (7)	C(41)-P/N-C(61)	113.3 (10)	111.3 (6)
S(21)-Ta/Nb-S(22)	81.54 (22)	78.76 (7)	C(41)-P/N-C(71)	106.9 (10)	111.5 (6)
S(21)-Ta/Nb-S(31)	88.89 (24)	103.32 (7)	C(51)-P/N-C(61)	108.7 (10)	112.4 (6)
S(21)-Ta/Nb-S(32)	164.30 (23)	105.59 (7)	C(51)-P/N-C(71)	112.0 (10)	110.6 (6)
S(22)-Ta/Nb-S(31)	104.63 (23)	159.38 (7)	C(61)-P/N-C(71)	107.1 (10)	105.8 (6)
S(22)-Ta/Nb-S(32)	88.16 (21)	79.64 (7)			

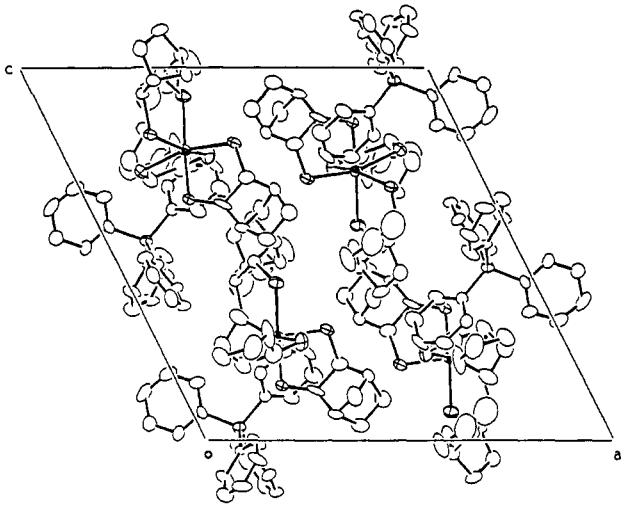

Figure 4. Packing diagram for $[Ph_4P][Ta(ndt)_3]$ (**2a**). The view is along the *b* crystallographic axis.

Et_4N; M = Nb, Ta), all of which comprise an MS_6 core having a pseudo D_3 local symmetry.

The situation is definitely different in the ndt complexes. As is evident in Figure 2 (top), the Ph_4P^+ salts (**1a** and **2a**) reveal as many as four peaks in the region, which is incompatible with a D_3 symmetry and the actual symmetry at the metal center of **1a** and **2a** must be lower. A plausible candidate is C_3 symmetry, which would give rise to two sets of IR active A and E normal M–S stretching modes. For Et_4N^+ (Figure 2, bottom), the MS_6 local symmetry should be still lower because there appear more than four peaks at 300–400 cm^{-1}. The X-ray derived solid-state structures of **2a** and **1b**, as will be shown in the following section, are consistent with these interpretations.

Solid-State Structure of $[Ph_4P][Ta(ndt)_3]\cdot CH_3CN$ (2a). Single crystals of **2a** are composed of discrete Ph_4P^+ cations, complex anions, and CH_3CN solvent molecules. An ORTEP drawing of the anion is shown in Figure 3, with the numbering scheme adopted, and a view of the molecular packing is given in Figure 4. No unusually short contacts between adjacent molecules or ions are seen. The closest among non-hydrogen atoms are N(1S) (x, y, z) in acetonitrile and C(76) (x, y, $-1 + z$) in Ph_4P^+, the separation being 3.25 (5) Å. The relevant bond distances and angles are listed in Table V (left).

In the complex anion of **2a**, three ndt ligands surround the tantalum(V) atom, where the coordination geometry formed by

Chart I

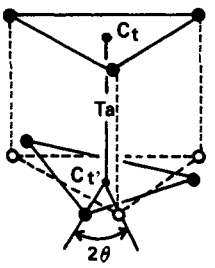

six sulfur atoms may be viewed as a distorted OH or a distorted TP. Thus the two trigonal faces defined by S11, S21, S31 and S12, S22, and S32 are nearly parallel, the dihedral angle between their normals being only 1.4°. The Ta atom is situated approximately on the line connecting the two triangle centers, C_t and C_t'. This is incarnated in the near-linear C_t–Ta–C_t' angle of 178.7°. The methylene bridge of each norbornane fragment orients in the same direction so that the anion has an approximate 3-fold axis along the C_t–Ta–C_t' spine. The individual chelate-twist angles (2θ) for the three ndt ligands, as shown in Chart I, are 37.6°, 39.5°, and 38.9°, with the average being 38.7°. They are larger than the other alkanedithiolate complexes of Nb, $[Et_4N][Nb(SCH_2CH_2S)_3]$ (av 30.5°) and $[Ph_4P][Nb(SCH_2CH_2CH_2S)_3]$ (18.5°), and are closer to the corrected octahedral twist (ca. 49°) based on the bidentate bite of $b = 1.31$[25] rather than to the trigonal-prismatic ideal of 0°. Interestingly, the three benzenedithiolate ligands in $[Ph_4As][Ta(S_2C_6H_4)_3]$ were reported to exhibit variegated twist angles of 16°, 16°, and 54°.[2d]

The S–Ta–S chelate bite angles of **2a** range from 81.5 (2)° to 82.5 (2)°, and their mean value of 82.1° compares well with 81° found in the structure of $[Ph_4As][Ta(S_2C_6H_4)_3]$. It is also similar to the S–Nb–S bite angles of $[Et_4N][Nb(SCH_2CH_2S)_3]$ (81.9°),[11b] $[Ph_4P][Nb(SCH_2CH_2CH_2S)_3]$ (83.5°),[11d] and $[Ph_4As][Nb(S_2C_6H_4)_3]$ (80.4°).[2e] The TaS_2C_2 chelate rings are not strictly planar but adopt the gauche configuration as a consequence of a slight tilt of the norbornane units with respect to the TaS_2 planes.

Although the Ta–S bond lengths of 2.398 (8)–2.435 (6) Å are not unusual,[2d,26] it is worth mentioning that they can be grouped

(25) Kepert, D. L. *Inorg. Chem.* **1972**, *11*, 1561–1563.

(26) (a) Schrock, R. R.; Wesolek, M.; Liu, A. H.; Wallace, K. C.; Dewan, J. C. *Inorg. Chem.* **1988**, *27*, 2050–2054. (b) Ta(V)–S(dialkyldithiocarbamate) distances are understandably longer. See: Peterson, E. J.; Von Dreele, R. B.; Brown, T. M. *Inorg. Chem.* **1978**, *17*, 1410–1415, and see also ref 23b.

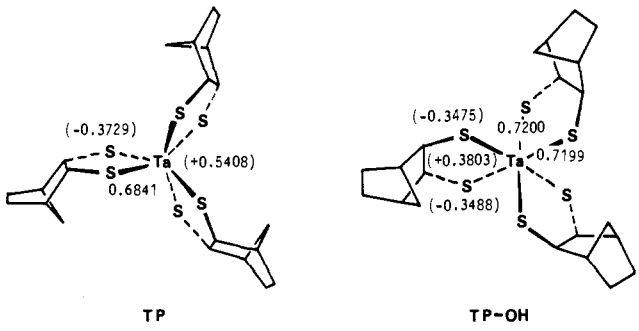

Figure 5. Ta–S overlap populations calculated for the TP and TP–OH (trigonal twist, $2\theta = 39°$) geometries of $[Ta(ndt)_3]^-$. The numbers in parentheses with signs are charges on the atoms nearby.

into three short and three long distances belonging to opposite triangle faces of sulfur atoms defined in Chart I. These are S(11)S(21)S(31) with Ta–S = 2.404 Å (av) and S(12)S(22)S(32) with Ta–S = 2.431 Å (av). In other words, coordination of each chelating ligand occurs with a pair of nonequivalent Ta–S distances. Due to the small but distinct distortion, symmetry of the TaS_6 frame is lowered from D_3 to C_3. We think this distortion accounts for the presence of four intense IR lines at 300–400 cm^{-1}, where each set of A and E bands arises from three Ta–S bonds within the same triad.

When the TaS_6 core deviates from TP to OH, as is the case of **2a**, two sulfur atoms of each ndt ligand in the complex are a priori nonequivalent in the sense that one sulfur comes closer to the methylene bridge of another ndt ligand. For instance, the S(11)–H(37A) distance of 3.18 Å is evidently shorter than the S(12)–H(37A) distance of 4.99 Å.

In order to examine whether this unsymmetric environment at the ndt ligands does really cause the observed C_3 distortion, we performed extended Hückel calculations on $[Ta(ndt)_3]^-$ with synclastic configuration, D. In the calculations, the TaS_2C_3 rings are assumed to be planar, and the coordination geometry at Ta is either an ideal TP (C_{3h}, $2\theta = 0°$) or the one modeled after the observed structure with the trigonal-twist angle of $2\theta = 39°$. Other geometrical and computational details are given in the Experimental Section. The calculated Ta–S overlap populations, which are shown in Figure 5, tend to increase as the complex twists from $2\theta = 0°$ to $2\theta = 39°$. At the same time, charges on the sulfur atoms become less negative, −0.373e at $2\theta = 0°$ vs −0.348e and −0.349e at $2\theta = 39°$, implying that such trigonal deformation from TP makes the Ta–S bonds more covalent. We note here that the rather modest decrease in negative charge of each of the six S atoms leads to a substantial drop of positive charge on the metal. The change in the Ta–S bond character, however, occurs to nearly the same extent for the two sulfur atoms in each ndt ligand. Thus, according to our calculations, no electronic reason for nonequivalent of Ta–S bonds upon coordination is discernible.

Solid-State Structure of $[Et_4N][Nb(ndt)_3]$ (1b). Figure 6 presents ORTEP drawings of the $[Nb(ndt)_3]^-$ anion and of its NbS_6 portion, and Figure 7 shows the crystal-packing diagram. Again, there exist no unusual interionic interactions in the lattice. The shortest contact of non-hydrogen atoms occurs between C(34) (x, y, z) in $[Nb(ndt)_3]^-$ and C(72) (x, $-y$, $-1/2 + z$) in Et_4N^+, with the separation being 3.55 (2) Å. Selected metric data within each ion are compiled in Table V (right).

One obvious feature seen in the structure of $[Nb(ndt)_3]^-$ in **1b** is that one ndt ligand on Nb orients in the direction opposite to the other two in the periphery of the coordination sphere. This contrasts to the propeller-type synclastic configuration found for **2a**. In the less orderly ligand arrangement, the chelate-ring conformations of the three ndt ligands in **1b** are evidently different. The NbS(31)C(31)C(32)S(32) ring is nearly planar wherein the largest deviation from the least-squares plane is negligible 0.036 Å, while the other NbS_2C_2 chelate rings are folded around the S–S axes. The folding angles between NbS_2 and S_2C_2 planes are 141.6° and 130.9° for NbS(11)C(11)C(12)S(12) and NbS(21)C(21)C(22)S(22), respectively. The chelate bite angles also

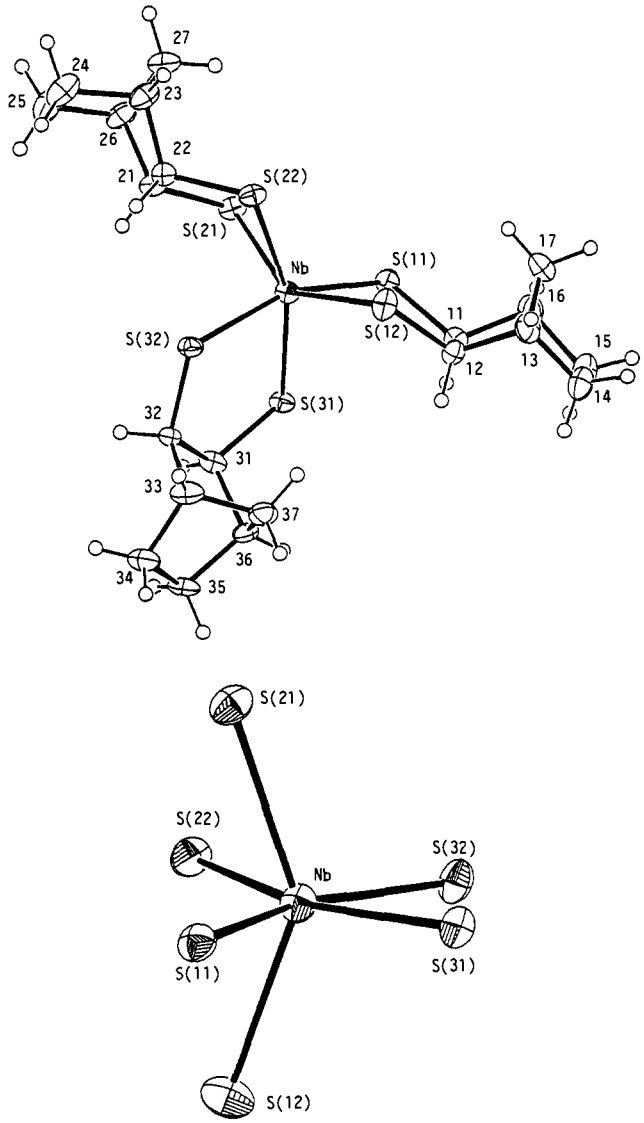

Figure 6. ORTEP views of the anticlastic $[Nb(ndt)_3]^-$ anion of **1b**, drawn at the 50% probability level, with the atom-labeling scheme: (top) top view of the entire anion; (bottom) the NbS_6 coordination sphere from the side emphasizing the BCT geometry.

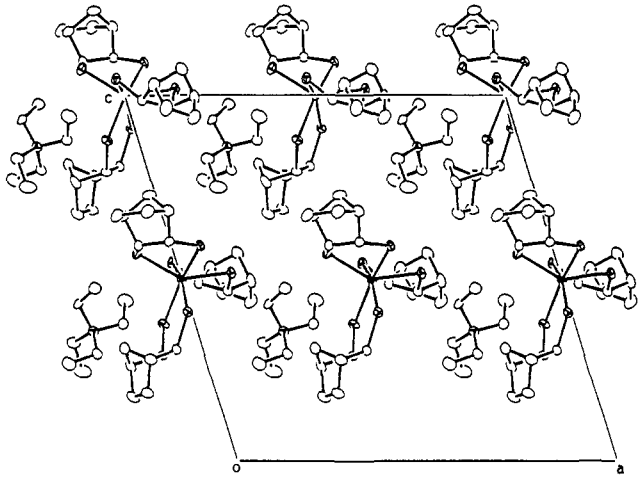

Figure 7. Packing diagram for $[Et_4N][Nb(ndt)_3]$ (**1b**). The view is along the b crystallographic axis.

vary from 78.76 (7)° to 81.37 (7)°. Consequently, the NbS_6 coordination geometry departs substantially from OH or TP and cannot be described in terms of trigonal distortion therefrom, either. As a matter of fact, the upper S(12)S(22)S(32) triangular

Table VI. Overlap Populations Calculated for the Five Limiting Geometries of $[Nb(ndt)_3]^-$

	synclastic		anticlastic		
	G (TP)	H (TP-OH)[a]	I (TP)	J (BCT)[b]	K (BCT')[c]
P(Nb–S(11))	0.6778	0.7134	0.6776	0.6484	0.6345
P(Nb–S(12))	0.6778	0.7131	0.6776	0.7068	0.6934
P(Nb–S(21))	0.6778	0.7134	0.6779	0.7070	0.6793
P(Nb–S(22))	0.6778	0.7131	0.6779	0.6486	0.6247
P(Nb–S(31))	0.6778	0.7134	0.6781	0.7203	0.7311
P(Nb–S(32))	0.6778	0.7131	0.6781	0.7200	0.7414
P(S--S)[d]	−0.3462	−0.2568	−0.3466	−0.3176	−0.2863

[a] Twist angle (2θ) defined in Chart I is 39°. [b] The NbS_2C_2 chelate rings are planar. [c] Two NbS_2C_2 rings are folded as in **1b**. [d] The sum of all S--S nonbonded interactions.

face does not parallel the lower S(11)S(21)S(31) face, and they tilt by 14.8°.

Instead, the NbS_6 frame is better viewed as an OH distorted toward a bicapped tetrahedral geometry (BCT) as shown in Figure 6 (bottom). In the BCT description, S(12), S(21), S(31), and S(32) make up tetrahedral parentage, with S(11) and S(22) being situated at capping positions. The distinct coplanarity of Nb, S(11), S(22), S(31), and S(32) (maximum deviation, 0.06 Å), and concomitant perfect perpendicularity between the equatorial plane and the NbS(12)S(21) plane (90.0°) conform to a BCT configuration derived from nontrigonal deformation of OH. On the other hand, the S(11), S(12), S(21), and S(22) atoms are decidedly nonplanar. Deviations from the mean plane are 0.20 Å with diagonal atoms having the same sign of displacement from the plane. In terms of the bond angles, S(21)–Nb–(12) (142.26 (8)°) and S(32)–Nb–S(31) (80.07 (7)°) angles do not reach the ideal tetrahedral value. Yet, the overall NbS_6 configuration is impartially classified as a BCT.

As a result of the nontrigonal distortion, the observed Nb–S bond lengths are diverse, ranging from 2.398 (2) Å (Nb–S(32)) to 2.488 (3) Å (Nb–S(22)) with the average being 2.439 Å.[2e,11b-e,27] No wonder the IR spectrum of **1b** shows many peaks arising from Nb–S stretching vibrations! Such an unusually wide range in Nb–S bond lengths may be compared with those of the related dithiolate complexes of Nb, which are 2.425 (1)–2.4422 (9) Å (av 2.434 Å) in $[Et_4N][Nb(SCH_2CH_2S)_3]$, 2.442 (4)–2.466 (4) Å (av 2.450 Å) in $[Ph_4P][Nb(SCH_2CH_2CH_2S)_3]$, and 2.428 (2)–2.458 (2) Å (av 2.441 Å) in $[Ph_4As][Nb(S_2C_6H_4)_3]$. Particularly noteworthy is that shortening of Nb–S bonds occurs in the planar NbS(31)C(31)C(32)S(32) chelate ring, with the Nb–S bonds at the capping sites being elongated.

Although in a recent molecular orbital analysis d^0 TiR_6^{2-} (R = H, CH_3) have a substantial preference for the BCT geometry, experimental evidence for existence of stable d^0 BCT structures is scarce. Thus the distortion observed in the coordination geometry of **1b** provides us with a good opportunity to test the validity of the theoretical predictions. It also has some heuristic values, for it may induce people to recognize the importance of BCT as another key d^0 six-coordinate geometry.

According to the theoretical study by Jean and Eisenstein, d^0 TiX_6^{2-} complexes favor the BCT geometry over the ideal OH when X is a σ-donor ligand, while with a π-donor ligand (e.g., X = Cl), TiX_6^{2-} tends to remain octahedral.[9] With these facts in mind, we consider the following five limiting geometries of $[Nb(ndt)_3]^-$; G (synclastic, TP), H (synclastic, TP–OH), I (anticlastic, TP),

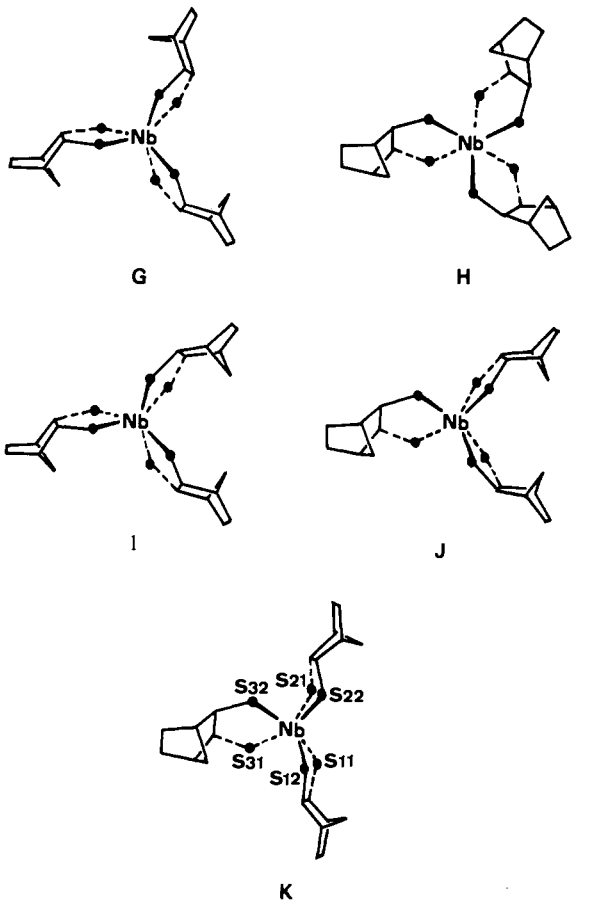

J (anticlastic, BCT), and K (anticlastic, BCT'). G and H correspond to geometries shown in Chart I with the trigonal-twist angles of $2\theta = 0°$ and $2\theta = 39°$, respectively, where the three ndt ligands assume the synclastic orientation. On the other hand, nontrigonal deformation of anticlastic $[Nb(ndt)_3]^-$ is represented by motion from I to J, where the latter NbS_6 configuration mimics that of **1b** while planarity of all the NbS_2C_2 chelate rings is retained. Finally, in K the two NbS_2C_2 rings are folded as in **1b** (see Figure 6). Our analysis consists of an inspection of overlap populations (*P*) for the Nb–S bonds as well as those for S--S nonbonded interactions. Comparison of these quantities *P*(Nb–S) and *P*(S--S) is made in Table VI.

Focusing on the sum of S--S overlap populations, we find that the two orientations of ndt ligands in the TP geometry (G and I) give nearly the same *P*(S--S) values and that they become less negative from G to H and from I to J to K. The congestion of S-donor atoms at the metal center appears to be relieved by either trigonal or nontrigonal distortion. Interestingly, folding of the two chelate rings in K is also effective in easing the S--S repulsion. For all the geometries under consideration, there are no short contacts between norbornane skeletons.

In regard to the Nb–S bonds, trigonal twist of synclastic $[Nb(ndt)_3]^-$ from G to H increases the *P*(Nb–S) values uniformly. This is analogous to the change in *P*(Ta–S) of $[Ta(ndt)_3]^-$ shown in Figure 5. In the case of nontrigonal deformation (I to J) of anticlastic $[Nb(ndt)_3]^-$, the Nb–S bond strength is differentiated in such a way that *P*(Nb–S) of each capping site is relatively small and those of the sterically freer sites largest. This trend is magnified by the NbS_2C_2 ring folding in going from J to K. The increasing order of Nb–S overlap populations mirrors very well the order of the observed bond lengths in the structure of **1b**. The range of *P*(Nb–S) for K can be rationalized in terms of different degrees of Nb–S π-interactions.[28] A crucial Nb orbital is the

(27) (a) Sulfides bridged between two Nb(III) centers in $Cp_2Nb_2(\mu\text{-}S)_2(CO)_4$, and those between two Nb(IV) centers in $Cp_2Nb_2(\mu\text{-}S)_3(CO)_4$ have the Nb–S distances of 2.520 (2)–2.648 (3) Å, while the Nb(II)–$(\mu\text{-}SCH_3)$ distances in $Cp_2Nb_2(\mu\text{-}SCH_3)_2(CO)_4$ are 2.548 (11)–2.579 (12) Å. See: Herrmann, W. A.; Biersack, H.; Ziegler, M. L.; Balbach, B. *J. Organomet. Chem.* **1981**, *206*, C33–C37. (b) Nb(V)–S(dialkyldithiocarbamate) distances are also long ranging from 2.517 (5) to 2.707 (3) Å. See ref 23b. (c) Nb(IV)–$(\mu$-S) distances in $Nb_2X_4(S)(S_2)\cdot 4tht$ (tht = tetrahydrothiophene; X = Cl, Br) are very short, 2.225 (15)–2.336 (10) Å. See: Drew, M. G. B.; Baba, I. B.; Rice, D. A.; Williams, D. M. *Inorg. Chim. Acta* **1980**, *44*, L217–L218.

(28) Importance of M–L π-interactions has been invoked in explaining the way in which some d^4 six-coordinate complexes are deformed from an ideal octahedron. See: Kubáček, P.; Hoffmann, R. *J. Am. Chem. Soc.* **1981**, *103*, 4320–4332.

vacant d_{xz} illustrated in L. The bent S(21)–Nb–S(12) spine in

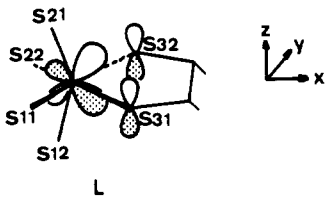

L

the BCT geometry induces the mixing of Nb p_z into d_{xz}, and the resulting "d_{xz}" orbital is hybridized toward S(31,32), which in turn enhances S(31,32) to Nb π-donation. The Nb–S π-interactions are maximized when the chelate ring is planar as it actually is in **1b**. In return, Nb–S(11,22) π-interactions are weakened most while Nb–S(12,21) interactions also suffer from the metal p–d hybridization. Folding of these two chelate rings further reduces the π-interactions. To put it another way, the BCT NbS_6 configuration makes Nb–S(11,12,21,22) π-interactions less important and thereby allows the two NbS_2C_2 rings to fold, thus relieving S--S repulsive interactions without a significant weakening of Nb–S bonds. This view gives a partial support to the theoretical prediction by Jean and Eisenstein in that a BCT structure is possible for d^0 MX_6^{2-} if π-donor ability of X is not significant.

Synclastic vs Anticlastic Configurations of $[M(ndt)_3]^-$ in Solid. The X-ray diffraction study has revealed that the norbornane-dithiolate complexes, $[M(ndt)_3]^-$ (M = Nb, Ta), can have either a synclastic or an anticlastic geometry in the solid. According to the IR spectra, the geometrical preference does not depend on the identity of the central metal, Nb or Ta, but is governed by countercations. When the cation is $[Ph_4P]^+$ or $[n\text{-}Bu_4N]^+$, the synclastic configuration of the anion is preferred, while with $[Et_4N]^+$ the alternative anticlastic configuration becomes feasible. Therefore, one may anticipate that stabilities of the two isomers of $[M(ndt)_3]^-$ by themselves would not differ much and the structural choice would be determined by a certain crystal-packing effect. In fact, as will be shown in the following chapter, the two isomers of either the Nb or the Ta complex coexist in solution with a statistical or nearly statistical distribution.

The presence or absence of crystal solvents is apparently not important, and we think the size of countercations relative to the complex anions controls the solid-state structures. If the ions are approximated to be spherical, their sizes can be conveniently measured by adding the van der Waals radius of hydrogen (1.2 Å) to the longest X--H distance within an ion, because the outermost atom is hydrogen for all the ions in question. Here, X stands for a central atom, i.e., Nb or Ta for $[M(ndt)_3]^-$, and N or P for the cations. The calculated "van der Waals radii" of ions, based on the X-ray structures of **1b** and **2a**, are 7.8 Å (anticlastic $[Nb(ndt)_3]^-$), 7.9 Å (synclastic $[Ta(ndt)_3]^-$), 6.8 Å ($[Ph_4P]^+$), and 4.5 Å ($[Et_4N]^+$). The corresponding value for $[n\text{-}Bu_4]^+$ was estimated to be in the range of ca. 6.5–7.3 Å depending on conformation of *n*-Bu chains. Thus, it is evident that $[M(ndt)_3]^-$, $[Ph_4P]^+$, and $[n\text{-}Bu_4N]^+$ are of similar size, while $[Et_4N]^+$ is substantially smaller.

According to these calculated van der Waals radii, we hypothesize that the highly symmetrical synclastic configuration is favored for $[M(ndt)_3]^-$ when the bulk of countercation matches that of anion and that the less symmetrical anticlastic geometry is promoted when the countercation is markedly smaller in size than the anion. In the case of $[Et_4N]^+$, its size is sufficiently small to perturb anisotropically the coordination sphere of the complex anion, resulting in the less symmetrical anticlastic $[M(ndt)_3]^-$ geometry.

Variable-Temperature ^1H NMR Study. Isolation of the two geometrical isomers of $[A][M(ndt)_3]$ (M = Nb, Ta) in the solid state prompted us to examine their solution behavior by ^1H NMR spectroscopy. As was mentioned earlier in this paper, we have measured variable-temperature ^1H NMR spectra for **1a**, **1b**, and **2a** in CD_2Cl_2 at low temperatures. In principle, the temperature dependences of all proton resonances associated with ndt ligands could be analyzed, but we monitor the fluxional behavior by using signals of the methine protons (H1) geminal to sulfur,[29] for they

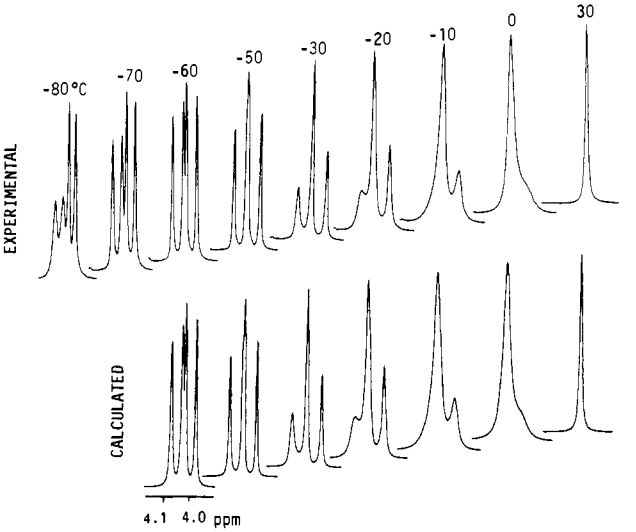

Figure 8. Variable-temperature ^1H NMR (400 MHz, in CD_2Cl_2) of $[Ph_4P][Ta(ndt)_3]$ (**2a**) in the methine (H1) region (top) and calculated spectra (bottom). See Table IV for the details of 30 °C spectra and atom numbering scheme.

are well isolated in the spectra and spin couplings with other protons are minimal.

The observed variable-temperature 400-MHz spectrum at around 4 ppm for **2a** is shown in Figure 8 (top). At 30 °C the methine (H1) region consists of a slightly broad singlet and the long-range coupling to H6 is masked, where the coupling constant (~2 Hz) can be measured using 100-MHz ^1H NMR. As the temperature is lowered, the singlet undergoes further broadening followed by emergence of four resonances at −60 °C. At even lower temperatures the two downfield peaks begin to broaden again. This behavior is indicative of two types of environmental averaging processes, which are probably intramolecular in origin. The spectral change associated with the high-temperature process must arise from interconversion between the synclastic and anticlastic isomers that seem to coexist in solution. Thus one H1 resonance at −60 °C would corresponds to the synclastic isomer and the remaining three resonances to the anticlastic isomer. Then below ca. −60 °C the exchange of the two ndt methine (H1) protons geminal to sulfur starts to freeze out; they are geometrically nonequivalent in either of the isomeric forms as is evident in the X-ray structures of **1b** and **2a**.

In order to verify the above interpretation, we have simulated the spectral change over the temperature range −60 to +30 °C (high-temperature process) with a DNMR5 program, assuming that the isomerization is described by a single independent rate parameter k_I. Since the chemical shifts of the H1 signals are markedly temperature dependent, those used in analysis were obtained by a linear or a smooth nonlinear extrapolation as indicated by the dashed lines in Figure 9. The average of the extrapolated shifts agreed to within 0.6 Hz of the observed fast-exchange shift. Simulations of the analogous spectral changes for **1a** (−60 to +30 °C) and **1b** (−70 to +30 °C) were performed in a similar manner. The effect of spin coupling with the H6 proton was included in our analysis, which affected only slightly the 30 °C spectra for **2a**, whereas in the case of **1a** and **1b** such an effect was found important to the line shapes at 10–30 °C. The spectra calculated therefrom for **2a** are given in Figure 8 (bottom). The rate parameter k_I at each temperature was estimated from visual comparison of computed and experimental spectra.

Before going into rates of synclastic $\rightleftharpoons$ anticlastic interconversion, we briefly comment on the mole fractions of the two isomers in CD_2Cl_2. On the basis of the line-shape analysis for the H1 protons, the downfield resonance of the −80 to −20 °C

(29) See Table IV for assignments of the ^1H NMR signals of the 30 °C spectra and the atom numbering scheme.

Scheme II

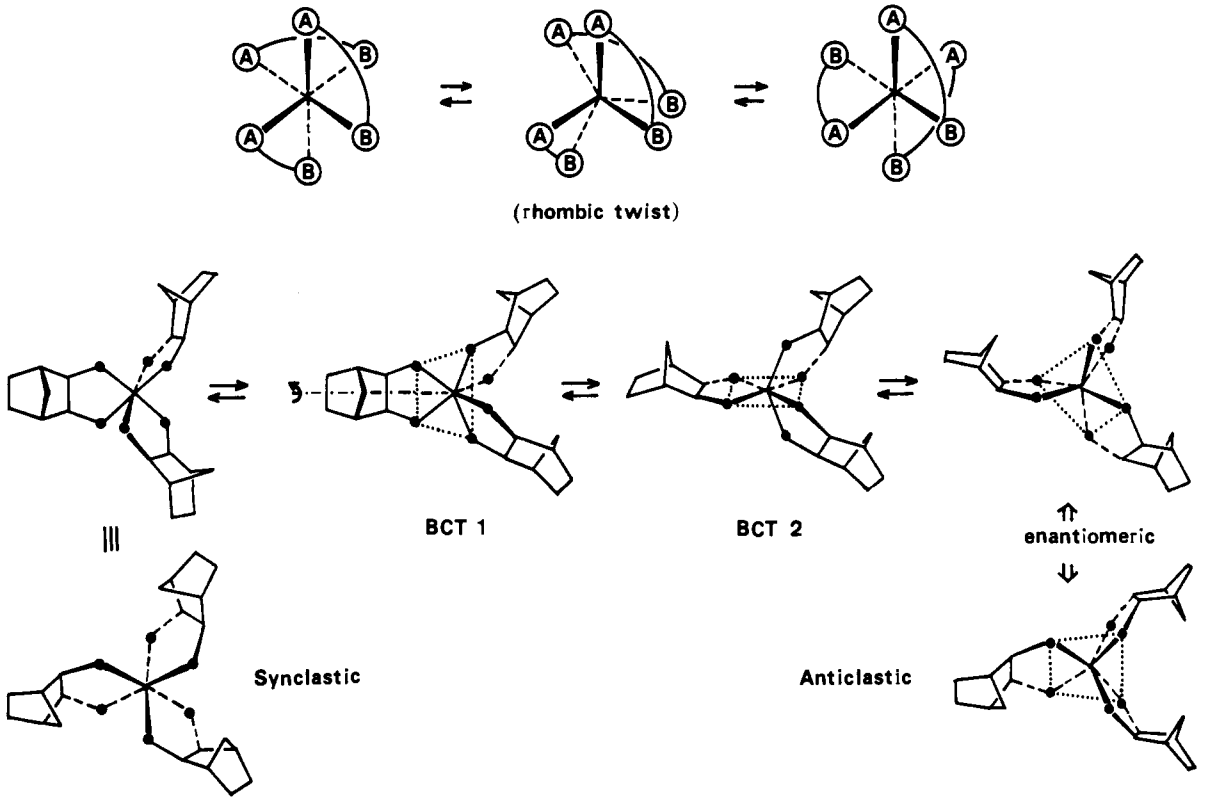

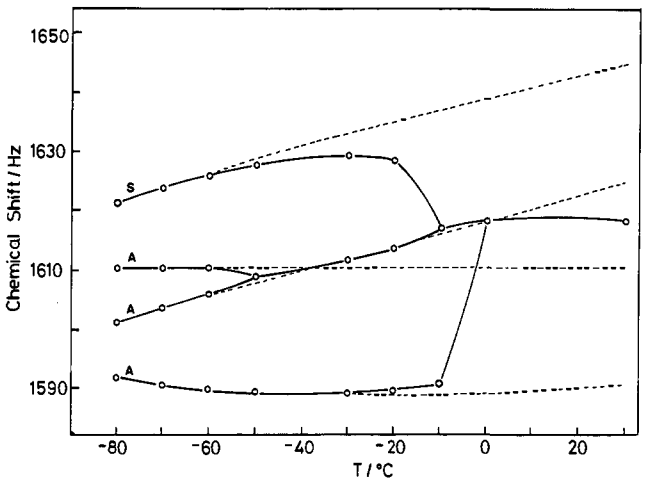

Figure 9. Temperature dependencies of the chemical shifts of the H1 signals for synclastic (S) and anticlastic (A) isomers of $[Ph_4P][Ta(ndt)_3]$ (**2a**) in CD_2Cl_2.

spectra of **2a** was assigned to its synclastic signal.[30] Unfortunately, we were unable to determine thermodynamic parameters for the equilibria, because the low-temperature process perturbs the spectra below ca. −50 °C and slow-exchange spectra are lacking.[31] However, we note here that the successful line-shape analysis for **2a** was achieved when the nuclear configurations derived from the synclastic and one of the three equivalent anticlastic ligand arrangements were assumed to be nearly equally populated (1/1–1.1/1). This holds true for **1a** and **1b** as well. Therefore, the ndt complexes form a statistical (1:3 synclastic–anticlastic) or nearly statistical distribution of isomers in solution,[32] and they do not show significant geometrical preference nor steric constraint in either isomeric form. This is consistent with our molecular orbital study described in the previous section.

Figure 10 displays Arrhenius plots for interconversion of **1a**, **1b**, and **2a**. Activation energies (E_a) and preexponential factors (A), as well as enthalpy and entropy changes of activation obtained by least-squares best fits of the kinetic data to the Eyring equation, are summarized in Table VII.[33] Careful and indeed elegant mechanistic studies of cis ⇄ trans isomerization are available for some tris-chelate complexes of Al and Co^{III}, etc., derived from unsymmetrically substituted bidentate O-donor ligands such as bzac, tfac, α-C_3H_5T, α-C_3H_7T, and pmhd, etc.[34-36] Although the origin of dissymmetry of such ligands differs from that of ndt, several useful comparisons of activation parameters can be made. The E_a values for cis ⇄ trans isomerization of the Al and Co complexes, which have been thought to occur via bond-rupture pathways, are generally quite high, ranging from 16.9 kcal/mol ($Al(\alpha\text{-}C_3H_5T)_3$) to 28–30 kcal/mol ($Al(pmhd)_3$) and from 15.5 kcal/mol ($Co(\alpha\text{-}C_3H_5T)_3$) to 32–33 kcal/mol ($Co(bzac)_3$). They are in marked contrast to the low E_a values observed for the ndt complexes of Nb and Ta, where the Nb complexes are slightly more mobile. The source of the difference between Nb and Ta

(30) The downfield resonances of H1 protons of the Nb complexes at −70 to −50 °C (**1a**) and at −85 to −50 °C (**1b**) were assigned also to their synclastic isomers.

(31) Above −40 °C, the transverse relaxation times (T_2) in the absence of exchange are fixed at 0.6 s, although they may be temperature dependent by themselves. Below −50 °C, however, four H1 signals are already broadened to different degrees because the low-temperature process starts to perturb the spectra, so that we were forced to employ smaller T_2 values of 0.2–0.25 s for our simulation of low-temperature spectra under such circumstances that slow-exchange spectra in terms of the low-temperature process is lacking.

(32) This situation occurs for most of the tris(β-diketonato) complexes of Co(III) and other trivalent metal ions. See ref 35 and 36.

(33) The probable errors in k_1 values estimated from the range of acceptable k_1's for a given temperature are less than ca. 5%.

(34) Key: Bzac, benzoylacetonate; tfac, (trifluoroacetyl)acetonate; α-C_3H_5T and α-C_3H_7T, α-isopropenyl- and α-isopropyltropolonate; pmhd, 1-phenyl-5-methylhexane-2,4-dionate.

(35) (a) Fay, R. C.; Piper, T. S. *Inorg. Chem.* **1964**, *3*, 348–356. (b) Fay, R. C.; Girgis, A. Y.; Klabunde, U. *J. Am. Chem. Soc.* **1970**, *92*, 7056–7060. (c) Girgis, A. Y.; Fay, R. C. *J. Am. Chem. Soc.* **1970**, *92*, 7061–7072, and references therein.

(36) (a) Gordon, J. G., II; Holm, R. H. *J. Am. Chem. Soc.* **1970**, *92*, 5319–5332. (b) Hutchinson, J. R.; Gordon, J. G., II; Holm, R. H. *Inorg. Chem.* **1971**, *10*, 1004–1017. (c) Eaton, S. S.; Holm, R. H. *J. Am. Chem. Soc.* **1971**, *93*, 4913–4914. (d) Eaton, S. S.; Hutchinson, J. R.; Holm, R. H.; Muetterties, E. L. *J. Am. Chem. Soc.* **1972**, *94*, 6411–6426.

Table VII. Activation Parameters for the Synclastic ⇄ Anticlastic Interconversion of **1a**, **1b**, and **2a** in CD_2Cl_2

complex	ln A	E_a, kcal/mol	$\Delta G^{\ddagger}_{303°}$, kcal/mol	$\Delta H^{\ddagger}$, kcal/mol	$\Delta S^{\ddagger}$, eu
$[Ph_4P][Nb(ndt)_3]$ (**1a**)	23.1 ± 0.7	9.1 ± 0.4	13.1	8.6 ± 0.4	−14.4 ± 1.5
$[Et_4N][Nb(ndt)_3]$ (**1b**)	24.4 ± 0.9	9.6 ± 0.5	12.6	9.2 ± 0.5	−11.5 ± 1.8
$[Ph_4P][Ta(ndt)_3]$ (**2a**)	25.7 ± 0.9	11.5 ± 0.4	13.7	11.1 ± 0.5	−8.8 ± 1.8

[a] All errors are random errors estimated at the 99% confidential level (2.5σ).

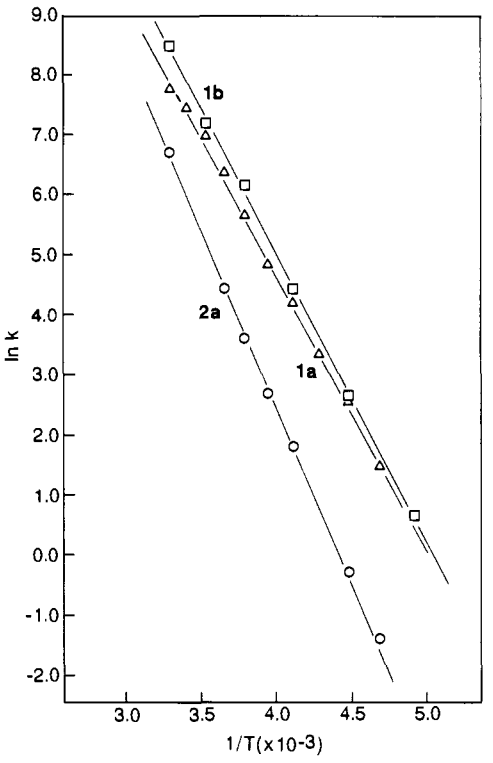

Figure 10. Arrhenius plots for the synclastic ⇄ anticlastic isomerization of $[Ph_4P][Nb(ndt)_3]$ (**1a**), $[Et_4N][Nb(ndt)_3]$ (**1b**), and $[Ph_4P][Ta(ndt)_3]$ (**2a**) in CD_2Cl_2.

is unclear at the moment, but the result is not inconsistent with the relatively rigid nature of $Rh(\alpha\text{-}RT)_3$ (R = α-C_3H_5, α-C_3H_7) compared to nonrigidity of $Co(\alpha\text{-}RT)_3$ and also with the fact that the barriers to polytopal rearrangement of $MH(PF_3)_4$ complexes increase uniformly in going from first- to second- to third-row elements, viz., Co < Rh < Ir and Ru < Os.[35b,36d,37]

(37) Meakin, P.; Jesson, J. P.; Tebbe, F. N.; Muetterties, E. L. *J. Am. Chem. Soc.* **1971**, *93*, 1797–1799.

It is not possible to elucidate the detailed mechanism of interconversion from our limited kinetic data alone.[38] Nonetheless, we prefer non-bond-rupture pathways because of the observed low-activation energies that are in fact similar in size to those of the optical inversion process via trigonal-twist pathways for $Al(\alpha\text{-}RT)_3$ and $Al(pmhd)_3$. There is also a ^1H NMR evidence that inversion and diketonate R group exchange in $Ti(R'COCHCOR')_2(OR)_2$ proceed by a twist mechanism.[39] Some support for this proposal, but not a tangible one, might be obtained from the low preexponential factors and negative activation entropies in Table VII.[40]

Non-bond-rupture mechanisms for cis ⇄ trans isomerization of octahedral $M(A\text{–}B)_3$ is usually thought to involve a rhombic twist (Scheme II, top). Perhaps this is more assumed than proven. Provided that the BCT structure of anticlastic $[M(ndt)_3]$ in solid is retained in solution, we may modify the rhombic-twist pathway to the one delineated in Scheme II (bottom) where BCT geometries are emphasized also at way points. This pathway does not differ in topology from the original rhombic twist but may have a pedagogical value. An essential part is the 90° rotation of one ndt ligand in going from BCT 1 to BCT 2, during which the other ndt's remain occupying the basal positions of a local square-pyramidal structure. Like the rhombic twist, the interconversion occurs with inversion of optical configuration.

Supplementary Material Available: Complete listings of anisotropic temperature factors of non-hydrogen atoms (Table S1) hydrogen atom parameters (Table S2) and bond lengths and angles (Table S3) (11 pages); observed and calculated structure factors for **2a** and **1b** (27 pages). Ordering information is given on any current masthead page.

(38) (a) Klemperer, W. G. *Inorg. Chem.* **1972**, *11*, 2668–2678; *J. Am. Chem. Soc.* **1973**, *95*, 2105–2120. (b) Musher, J. I. *Inorg. Chem.* **1972**, *11*, 2335–2340. (c) Beilar, J. C., Jr. *J. Inorg. Nucl. Chem.* **1958**, *8*, 165–175. (d) Modes of rearrangements in *cis*-$M(A\text{–}B)_2XY$ have been extensively studied. See, for example: William, R.; Gielen, M.; Pepermans, H.; Brocas, J.; Fastenakel, D.; Finocchiaro, P. *J. Am. Chem. Soc.* **1985**, *107*, 1146–1152, and references therein.

(39) Fay, R. C.; Lindmark, A. F. *J. Am. Chem. Soc.* **1983**, *105*, 2118–2127.

(40) Fortman, J. J.; Sievers, R. E. *Inorg. Chem.* **1967**, *6*, 2022–2029.